CHALMERS
UNIVERSITY OF TECHNOLOGY

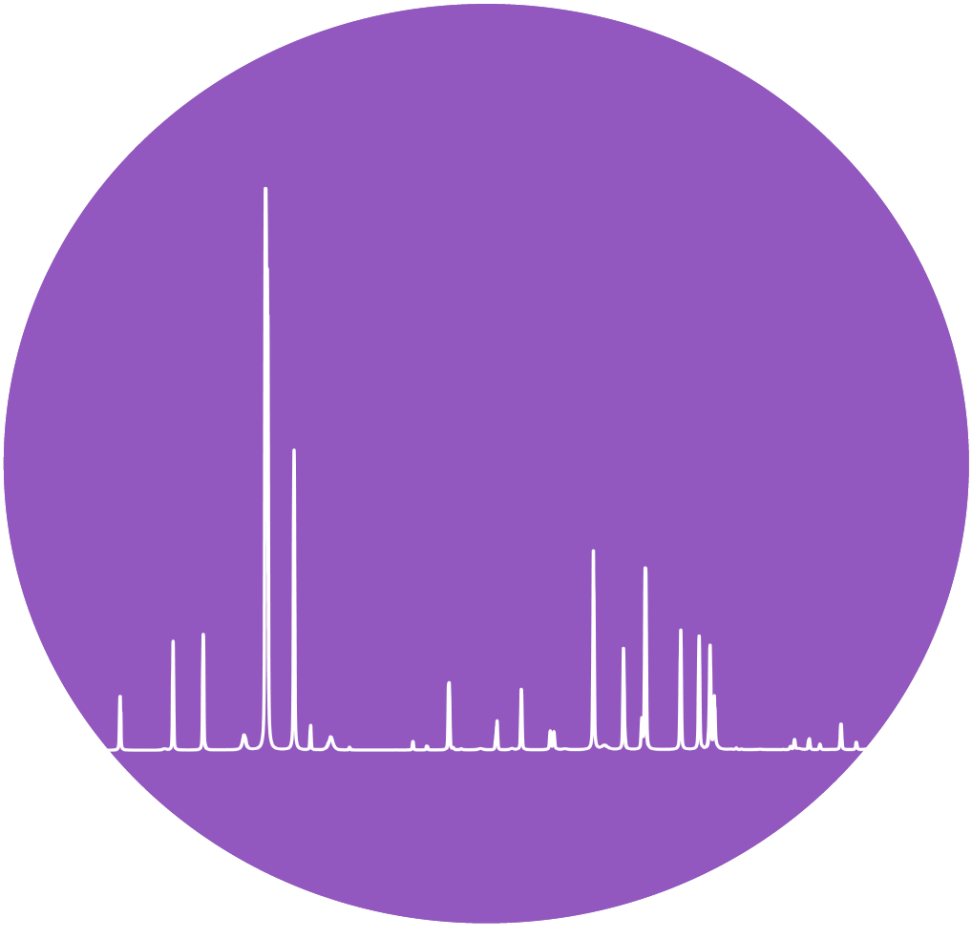

Copper-Doped Strontium Apatite

Synthesis and Structural Characterisation

Master's thesis in Nanotechnology

Pontus Ericstam

DEPARTMENT OF CHEMISTRY AND CHEMICAL ENGINEERING
Chalmers University of Technology
Gothenburg, Sweden 2026
www.chalmers.se

Master's thesis 2026

Copper-Doped Strontium Apatite

Synthesis and Structural Characterisation

Pontus Ericstam

CHALMERS
UNIVERSITY OF TECHNOLOGY

Department of Chemistry and Chemical Engineering
Division of Energy and Materials
Chalmers University of Technology
Gothenburg, Sweden 2026

Copper-Doped Strontium Apatite
Synthesis and Structural Characterisation
PONTUS ERICSTAM

Supervisor: Daniel Weber, Assistant Professor, Division of Energy and Materials, Department of Chemistry and Chemical Engineering
Examiner: Itai Panas, Full Professor, Division of Energy and Materials, Department of Chemistry and Chemical Engineering

Degree project report 2026
Department of Chemistry and Chemical Engineering
Division of Energy and Materials
Chalmers University of Technology
SE-412 96 Gothenburg
Sweden
Telephone +46 31 772 1000

Cover: PXRD pattern from synchrotron data on a 1400 °C sample. The purple background represents the sample's colour.

Typeset in LaTeX
Gothenburg, Sweden 2026

Copper-Doped Strontium Apatite
Synthesis and Structural Characterisation
PONTUS ERICSTAM
Department of Chemistry and Chemical Engineering
Chalmers University of Technology

Abstract

In this Master's thesis project, strontium apatite has been doped with copper ions using solid state synthesis methods. Different annealing temperatures and dwelling times were tested to see which synthesis conditions yielded the most phase pure sample. The composition and structure of the synthesised samples have been investigated using synchrotron powder X-ray diffraction with complementary Rietveld refinement. Infrared spectroscopy was used in order to investigate presence of OH-bonds in the structures. The results suggest that by annealing in air at 1400 °C for 6 hours, followed by air quenching, it is possible to achieve a purple-coloured copper-doped strontium apatite, with strontium phosphate being created as a minor side-phase. The infrared spectroscopy suggests no OH-bonds are present in the synthesised structures, and that some form of oxocuprate ions are present in the one-dimensional channels of the apatite structure. These results offer a relatively simple synthesis route, to be further optimised in order to achieve a phase pure sample of copper-doped strontium apatite. If achieved, the copper-doped strontium apatite could be used as a potential reference to copper-doped lead apatite, to see how the electron interactions differ between the two. The synthesis method could also be used as a platform for future investigations of how the structure and properties of apatites can be changed upon doping with copper, and potentially with other types of ions as well.

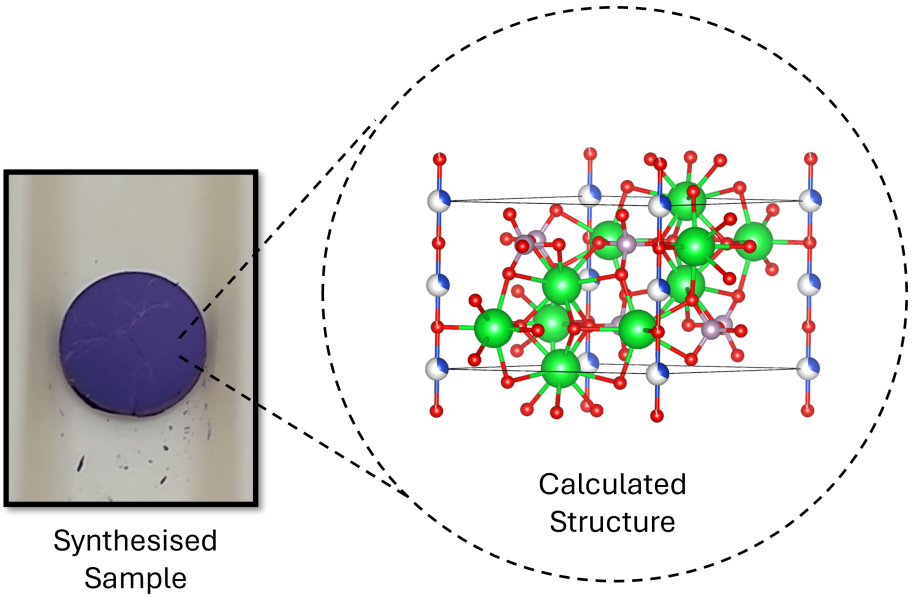

Acknowledgements

First of all, I would like to thank my supervisor Daniel Weber as well as examiner Itai Panas for the opportunity to perform a Master's thesis project in the interesting areas of solid state chemistry and apatites. Daniel has been of immense help when it came to perform solid state synthesis, learning the Rietveld Refinement method, as well as how to keep the project going when all the equipment didn't work as planned. Itai has also been an important support during the project, providing interesting theoretical discussions, as well as good ideas for tests to perform, in order to understand more about the synthesised material.

I have also had the pleasure to work with a great group of people in the Weber-lab with Shweta Dhiman, Raja Oubelhas, Iga Szpunar, Athira Anil, Kowsik Ghosh, Yicheng Liu, Parisa Kamalian, Erik Charles Smith, Waldemar Hult and Hampus Dahlberg. Everyone has been very helpful when it comes to learning the various machines and techniques in the lab, as well as making this into a very nice work environment in general. Thank you all - it has not been boring going to the office for the last couple of months.

A few other people I would like to thank are Torbjörn Jönsson from the mechanical workshop, for helping out with various tools, Dogac Tari and Elena Naumovska, for instructing how to use the furnaces on floor seven, and Pedram Pakmehr, for helping out with IR-measurements and data interpretation. The staff at Chalmers Materials Analysis Laboratory have also been of great guidance for learning how to use the PXRD - and IR instruments, as well as the staff at the Chalmers library for helping out with getting access to important references.

Edvin Martinson, Iga Szpunar, Job Winkel and Chalmers Writing Centre have all provided valuable feedback on the text, which I am very thankful for.

I also think this serves as a suitable occasion to thank you who came up with the idea of having education free of charge in Sweden, and to our study loan system, which are two things I have appreciated a lot.

Last, bur certainly not least, I would like to take the opportunity and express my gratitude to my family and friends, for all the support over the years, which I am very grateful for and lucky to have.

Pontus Ericstam, Gothenburg, March 2026

List of Acronyms

Below is a list of acronyms used throughout this text in alphabetical order:

CMAL	Chalmers Materials Analysis Laboratory
IR	Infrared
PXRD	Powder X–Ray Diffraction
VESTA	Visualisation for Electronic and STructural Analysis
CIF	Crystallographic Information File

Contents

List of Figures

List of Tables

Chapter 1

Introduction

In the introduction will a brief scientific background to this thesis project be presented, as well as the aim of the project. At the end is an outline of this text provided.

1.1 Background to the Project

The way in which electrons interact with each other is highly affected by the structure in which they reside, and can result in fascinating phenomena such as magnetism and superconductivity - superconductivity being the ability of a material to conduct electricity without energy loss, as well as expelling external magnetic fields [1]. The ability of a superconductor to expel external magnetic fields is known as perfect diamagnetism/the Meissner effect, and can result in a superconductor levitating when placed over a magnetic field.

Given the importance magnetism and superconductivity have in our society, in areas such as electric propulsion and medicine [2, 3], it is of interest to investigate and synthesise structures which can be tailored, in order to control the underlaying electronic interactions behind these phenomena.

In July 2023, Lee et al. reported to have discovered a material demonstrating superconductivity at room temperature and atmospheric pressure [4]. If this were to be true, it could have tremendous implications on our society, for example in terms of transporting electrical energy, since it would enable lossless conduction of electricity at record high temperatures. The material Lee et al. investigated was a copper-doped lead apatite, named *LK-99*, which had a proposed formula unit of $Pb_{10-x}Cu_x(PO_4)_6O$ ($0.9 \leq x \leq 1.1$). Several research groups quickly tried to replicate the room temperature superconducting phenomena in LK-99, although, none were successful [5, 6].

Instead, LK-99 was found to contain Cu_2S-impurities, and at 380 K (107 °C), Cu_2S undergoes a structural phase transition [7]. The result of this phase transition is a sharp drop in resistance, which Lee et al. originally thought manifested loss of electrical resistance in LK-99.

Samples of LK-99 were also found to partially levitate when placed over a magnet, originally thought to demonstrate the Meissner effect [8]. However, the magnetic levitation was discovered to be an effect of ferromagnetic impurities in LK-99 [9]. The claim of LK-99 showcasing superconductivity was thus refuted, but an increased interest regarding copper doped apatites had nonetheless been established.

A characteristic trait of apatites are one-dimensional channels present in their structure, usually consisting of anions such as O^{2-}- or F^{-}, surrounded by metal cations [10]. In the wake of the LK-99 debacle, I. Panas performed density functional theory (DFT) calculations on copper-doped lead apatite, where the Cu-ions were suggested to reside in these one-dimensional channels [11]. This is in contrast to the initial suggested structure of LK-99, where instead, Cu-ions were proposed to take the positions of lead ions [4]. It has also recently been demonstrated experimentally that Cu-ions are found in the one-dimensional channels when investigating single crystals of copper-doped lead apatites [12].

The DFT calculations by I. Panas showed that altering the amount of oxygen in copper-doped lead apatite, going from fully oxidised Cu(II) to fully reduced Cu(I), works as a method for tuning the electronic interactions in copper-doped lead apatite [11]. The DFT thus indicate a similar behaviour in copper-doped lead apatite as to how the electronic interaction can be altered in high temperature superconducting cuprates depending on the oxygen content [13].

It is however important to validate theoretical calculations by using real world experiments, and as a part of this, D. Weber and C. Geers performed initial synthesis on copper-doped *strontium* apatite. The idea being that copper-doped *strontium* apatite could be used as a potential reference material to copper-doped *lead* apatite, to see how their electronic interactions differ. This also marks the start of this thesis project, where the main focus is to synthesise copper-doped strontium apatite (CuSrApt) using solid state methods. Additionally, the copper-doped strontium apatite could be used as a model system for investigating doping-levels and oxygen content in apatites in general.

Comparing the strontium- and lead ion in their respective apatite structure, we have Sr^{2+} and Pb^{2+}, both with a similar ionic radius of 1.21 Å (Sr^{2+}) and 1.23 Å (Pb^{2+}) [14, 15]. The electron configuration differs however between the two ions, with Sr^{2+} having [Kr] and Pb^{2+} $[Xe]4f^{14}5d^{10}6s^2$. The similar radii, but lack of 6s electrons in Sr^{2+}, makes copper-doped strontium apatite suitable to be used as a reference, in order to investigate how the 6s valence electrons in Pb^{2+} affects the physical properties of copper-doped lead apatite.

1.2 Aim of the Thesis

The aim of this thesis project is to synthesise phase pure copper-doped strontium apatite, and determine its composition and structure. This will be done by evaluating synthesis parameters, such as annealing temperatures and dwelling times, in order to identify how these affect the obtained composition and structure. It will also be of interest to determine where the copper ions reside within the crystal structure, and how much of the copper that can enter the apatite structure.

1.3 Outline of the Thesis

Following chapters will start with providing important theoretical aspects of apatites and crystal structures in Chapter 2. In Section 2.1 is copper-doped strontium apatite specifically covered. The methods used in this project, and the theory behind them, is described in Chapter 3. Chapter 4 provides specifics for the experimental methods used, and in Chapter 5 are the obtained results presented and discussed. A summary of the main results, as well as an outlook for future studies can be found in Chapter 6. At the end of the text are the references provided, as well as the Appendix containing additional information from the Rietveld refinements.

Chapter 2

Apatites

The name "apatite", which denotes the crystal structure for a big class of minerals, can be derived from the Greek word *apatao*, meaning "to deceive" [16]. The origin of this being that apatite minerals for a long time were easily mistaken as other types of minerals. This changed however in the 18th century, when German mineralogist Abraham Werner recognised apatite as being its own type of mineral [16].

Historically, apatites have been used as gemstones [17], but the mineral has also been investigated for applications in bone replacement [18], handling nuclear waste [19], and in catalysis as well [20]. However, the biggest industrial use of apatites today is to synthesise fertilizers, since phosphorus is commonly found in apatite structures [21].

Regarding the apatite structure, it can be represented by the general formula $[A1]_4[A2]_6(MO_4)_6X_{2-y}$, with A1 and A2 being rare-earth, alkaline earth or alkali cations [22, 10]. M is a tetra - or pentavalent cation, and X is a di - or monovalent anion. The value of y will be ≤ 2, and is determined by the charge of the other ions in the structure.

If we consider hydroxyapatite as an example, which in fact is the main mineral constituent in our teeth and bones, we have both A1 and A2 = Ca^{2+}, M = P^{5+} and X = OH^- [23]. This simplifies the general apatite structure to $Ca_{10}(PO_4)_6OH_2$, or equivalently $Ca_5(PO_4)_3OH$ [24]. The difference between $Ca_{10}(PO_4)_6OH_2$ and $Ca_5(PO_4)_3OH$ being that the former corresponds to one unit cell of hydroxyapatite, whereas the latter correspond to the number of elements in one formula unit [25]. The difference between the A1 and A2 metal cations corresponds to which site they occupy in the hydroxyapatite unit cell, see Figure 2.1.

The symmetry of crystal structures is described by different space groups, of which 230 exists [1]. Each space group is denoted by a combination letters and numbers, describing the symmetrical traits of a specific crystal structure. In the case of the hydroxyapatite unit cell, its space group is the hexagonal $P6_3/m$. This symmetry means that hydroxyapatite has a primitive unit cell P, a 6_3 screw axis and mirror plane m. The $P6_3/m$ space group is in fact one of the most common space groups reported for apatite structures [22], but it is important to note that apatite structures are found in a variety of other space groups as well [22]. The structure of hydroxyapatite can be seen in Figure 2.1, and a visualization of the 6_3 screw axis in the $P6_3/m$ space group is presented in Figure 2.2.

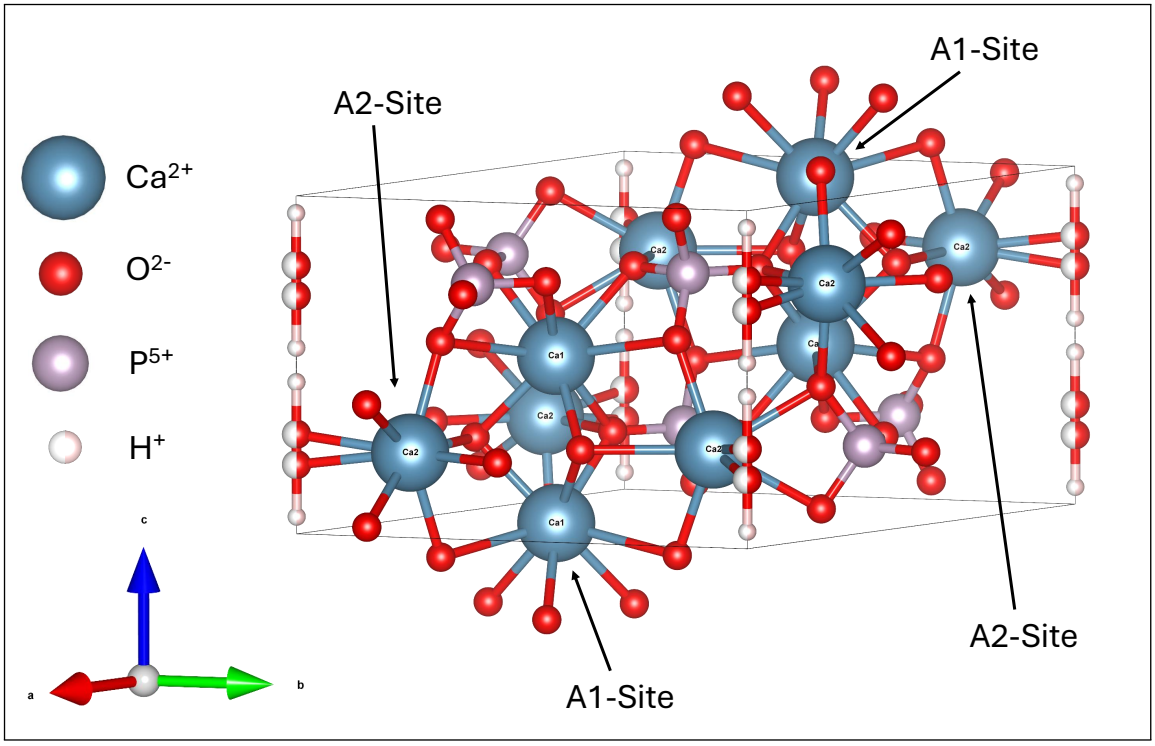

Figure 2.1: One unit cell of the hydroxyapatite, $Sr_{10}(PO_4)_6(OH)_2$, with cations on the A1- and A2-site marked. Visualised in VESTA from [26].

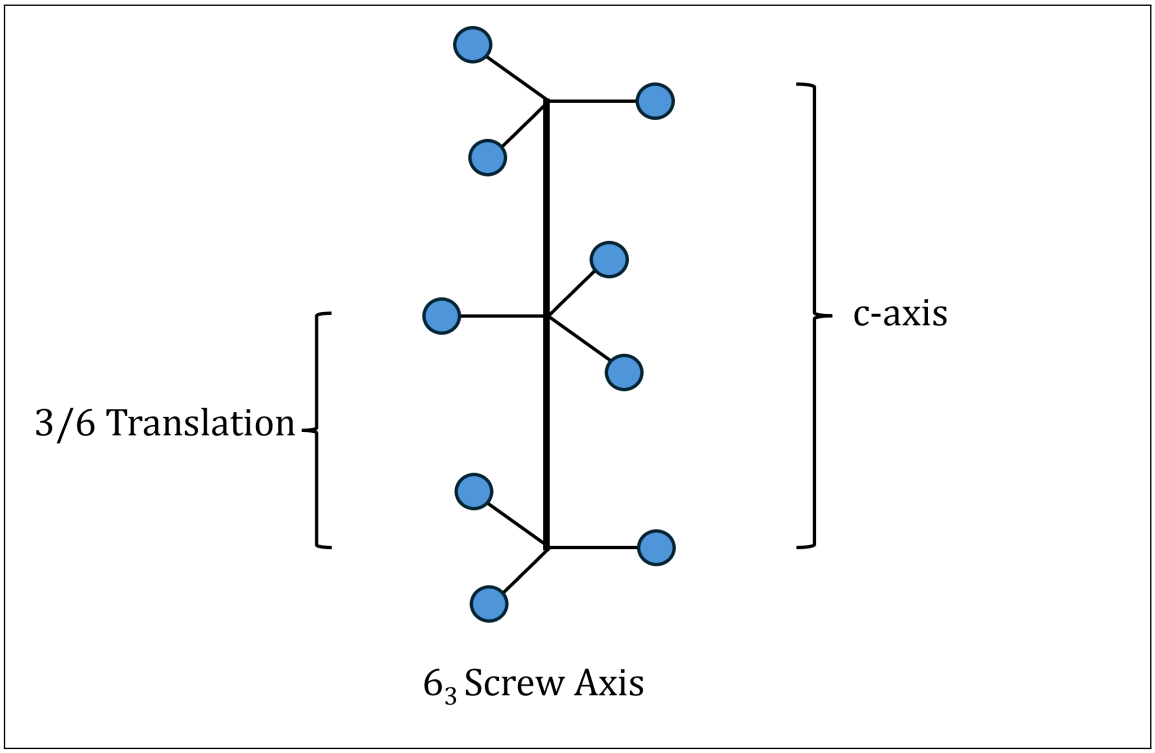

Figure 2.2: Visualisation of the 6_3 screw axis in the $P6_3/m$-space group. This screw axis also represents the surrounding to the one-dimensional channels in the apatite structure. The spheres correspond to cations on the A2-site in the apatite structure.

In Figure 2.3 are the characteristic one-dimensional channels along the c-axis in the apatite structure highlighted by green ovals. Note that in the case of hydroxyapatite, hydrogen and oxygen ions are located in theses channels, and that the occupancy of the oxygen and hydrogen positions is 50 %, represented by the hydrogen and oxygen spheres only being half-filled. This means that in reality, only half of the available oxygen and hydrogen positions are actually occupied by these ions.

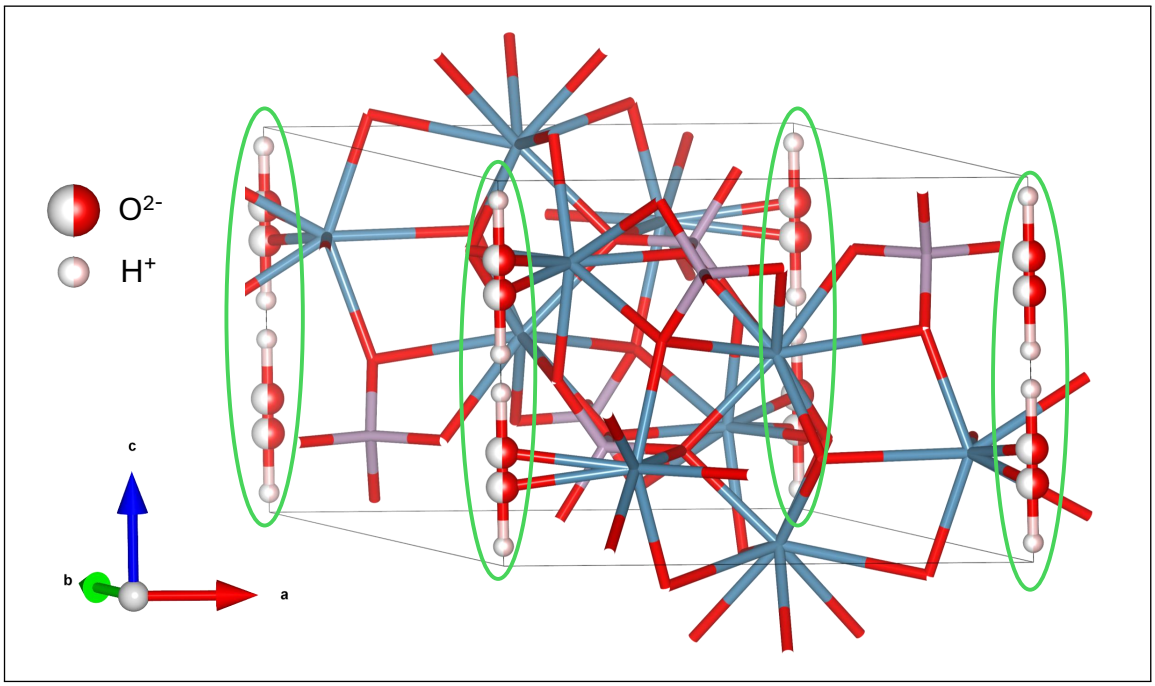

Figure 2.3: Green ovals highlighting the one-dimensional channels along the c-axis in hydroxyapatite, $Sr_{10}(PO_4)_6(OH)_2$. Visualised in VESTA from [26].

Figure 2.4 shows a supercell of hydroxyapatite from the c-axis. It can there be observed that the one-dimensional channels have a hexagonal shape, comprising of cations on the A2-position (Ca^{2+} in the case of hydroxyapatite).

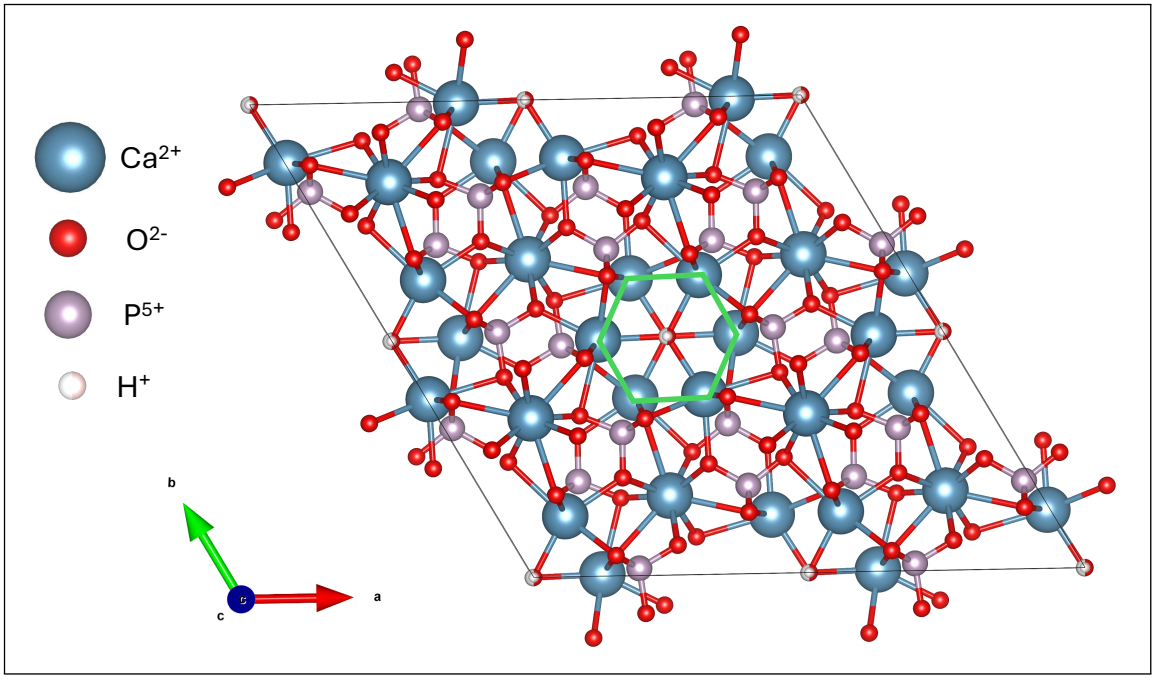

Figure 2.4: Supercell of hydroxyapatite viewed from the c-axis in VESTA. Note the hexagonal surrounding of the one-dimensional OH-channel in the middle, marked by the green hexagon. These channels with the hexagonal surrounding also manifest the $P6_3/m$ screw axis, and mare made up of cations on the A2-site. CIF-file from [26].

2.1 Copper-doped Strontium Apatite

Copper-doped strontium apatite (CuSrApt), can be seen as a strontium hydroxyapatite, $Sr_5(PO_4)_3OH$, where hydrogen in the one-dimensional channels is substituted against copper ions [27, 28]. The colour of CuSrApt has been reported to be blue-violet, and could possibly be used as a low toxic pigment [27, 28]. Reported synthesis methods include heating powders of strontium carbonate ($SrCO_3$), ammonium dihydrogen phosphate ($(NH_4)H_2PO_4$) and copper(II) oxide (CuO), followed by annealing at 1000 - 1100 °C and subsequent air quenching[1]. This synthesis method results in copper-doped strontium apatite where both hydrogen and copper is present in the one-dimensional channels [27, 28].

Single crystals of copper doped strontium apatite, without hydrogen present in the one-dimensional channels, have been synthesised using arc melting at approximately 1600-1700 °C [27]. This was done using copper-doped strontium apatite previously annealed at 1100 °C. The single crystal copper-doped strontium apatite has a proposed formula unit of $Sr_5(PO_4)_3(CuO_2)_{1/3}$, and $P6_3/m$ space group symmetry. Figure 2.5 shows the unit cell of $Sr_5(PO_4)_3(CuO_2)_{1/3}$, and in table 2.1 is the corresponding structural information for the different atomic positions in the unit cell provided. In $Sr_5(PO_4)_3(CuO_2)_{1/3}$, the one-dimensional channels are suggested to be comprised of linear oxocuprate ions, $[OCuO]^{3-}$, randomly distributed and separated by vacancies [27].

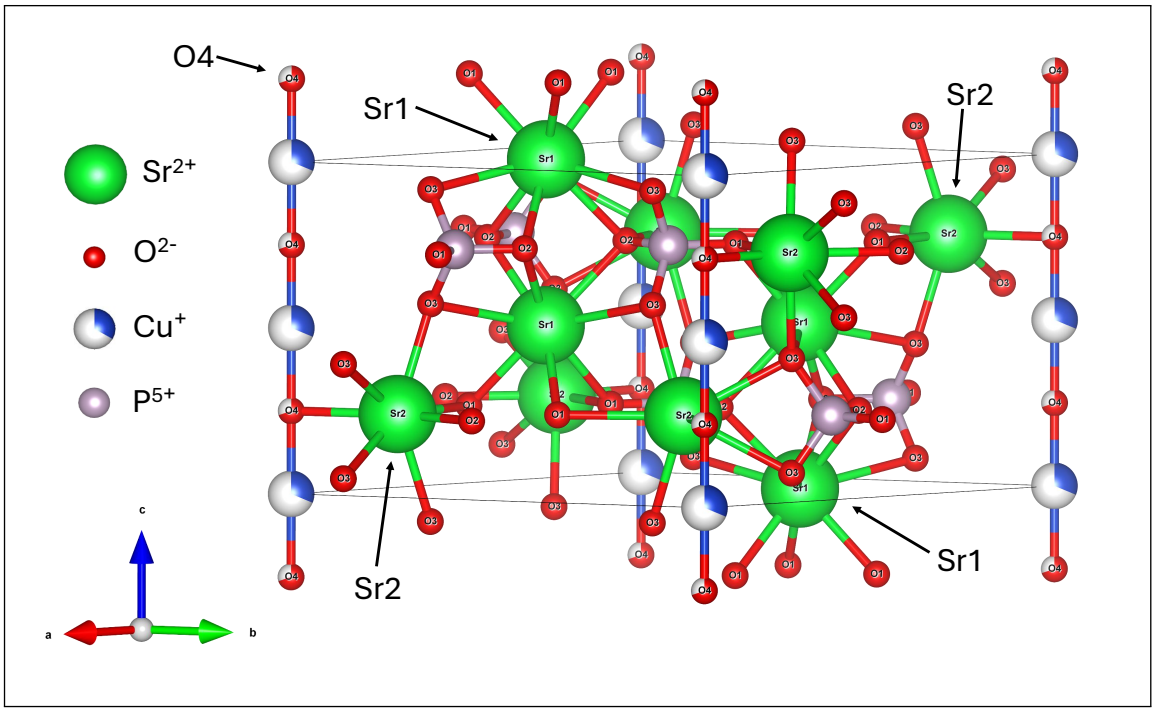

Figure 2.5: One unit cell of $Sr_5(PO_4)_3(CuO_2)_{1/3}$, where selected ions are marked with arrows. Visualised in VESTA from [27].

[1] Air quenching is the process of quickly cooling down a heated sample by moving it from the heated environment to the surrounding air.

Table 2.1: Coordinates, Wyckoff position and occupancies for the atoms in single crystals of $Sr_5(PO_4)_3(CuO_2)_{1/3}$. The site refers to which specific position a species in the unit cell it belongs to, with x, y and z being its coordinates in the unit cell. The occupancy denotes the degree to which a specific position is actually occupied by a species. The Wyckoff position describes the multiplicity and symmetry of a site in the unit cell [29]. The letter denoting how "high" the symmetry is for a specific site, with "a" corresponding to a position with higher symmetry than a "b"-site, and so. The number refers to the multiplicity of that site, that is, how many positions a specific atomic site generates in the unit cell. The numbers within the parenthesis correspond to the uncertainty in the given values. Data from [27]

Atomic Parameters						
Site	Species	Wyckoff Position	x	y	z	Occupancy
Sr1	Sr^{2+}	4f	1/3	2/3	0.00003(5)	1.0
Sr2	Sr^{2+}	6h	0.25929(4)	0.01428(4)	1/4	1.0
Cu	Cu^{+}	2b	0	0	0	0.314(4)
P	P^{5+}	6h	0.3678(1)	0.3997(1)	1/4	1.0
O1	O^{2-}	6h	0.4810(3)	0.3329(3)	1/4	1.0
O2	O^{2-}	6h	0.4619(3)	0.5820(3)	1/4	1.0
O3	O^{2-}	12i	0.2642(2)	0.3499(3)	0.0778(3)	1.0
O4	O^{2-}	2a	0	0	1/4	0.70(2)

Chapter 3

Methods

In this chapter is the key theoretical background presented behind the different experimental methods utilised in this project. First is the synthesis method used covered in Section 3.1. A brief overview of how X-rays are generated at a synchrotron facility is given in Section 3.2, and in Section 3.3 is the theory behind powder X-ray diffraction discussed. Section 3.4 and 3.5 provides important theoretical aspects of Rietveld refinement and infrared spectroscopy, respectively.

3.1 The Ceramic Method

The action of thoroughly mixing and heating reactants, usually ionic compounds, until they react, is referred to as the *high temperature ceramic method*, a method dating back at least 14 000 - 18 000 years ago [1, 30].

The goal of this method is to use heat in order to evaporate volatile components and let the non-volatile components react with each other. The reactions between the non-volatile components take place when enough energy is achieved so that the cations in the ionic compounds overcome the lattice energy holding them in place [1]. This means that the cations can leave their original position in a solid and start to diffuse, enabling them to react with other ions and form new bonds. High amounts of energy are needed to achieve this, leading to temperatures between 500 °C to 2000 °C typically being required. In addition to overcoming the lattice energy, high temperatures are used to speed up these reactions, since higher temperatures means the diffusion rate of the ions increases [1].

Apart from high temperatures, thorough grinding of reactants is of importance when performing solid state synthesis, since having reactants of a small particle size means the distance ions have to diffuse is decreased, speeding up the reaction [1]. Additionally, having well mixed reactants increases the contact surface area between them, being beneficial since it is between the interface of two solids that these reactions take place [1]. The surface contact area can further be increased by pelletising a powder of the reactants in a hydraulic press, leading to a greater amount of crystallite faces being in contact with each other.

The heating in solid state methods usually takes place in a resistance heating furnace as long as temperatures do not need to exceed 2000 °C [1]. This means that electrical energy is converted to heat as a result of the electrical resistance in a metallic element. During heating, the reactants are typically put in an inert and heat-resistant crucible, for example aluminium oxide- or platinum crucibles, which have

operating temperatures up to around 1900 °C and 1700 °C respectively [1].

There are several different ways to investigate the structure of synthesized materials. A common method is X-ray diffraction, and for that X-rays need to be generated, which will be the topic of the next section.

3.2 Synchrotron Generation of X-rays

A typical laboratory set-up generates X-rays by heating a metal filament until it emits electrons, and then accelerates them onto a metal target, with X-rays being produced as a result. A synchrotron facility however, exploits the fact that electromagnetic radiation can be generated as result of changing charge densities in the electromagnetic field [31]. This is achieved by accelerating charged particles in a circular path, creating what is known as synchrotron radiation [32]. This type of radiation provides a source of highly collimated, high intensity X-rays, with a more narrow energy distribution, compared to a standard laboratory X-ray source [32]. Useful benefits of these traits is the high signal-to-noise ratio and high resolution the synchrotron source X-rays provide [32, 33].

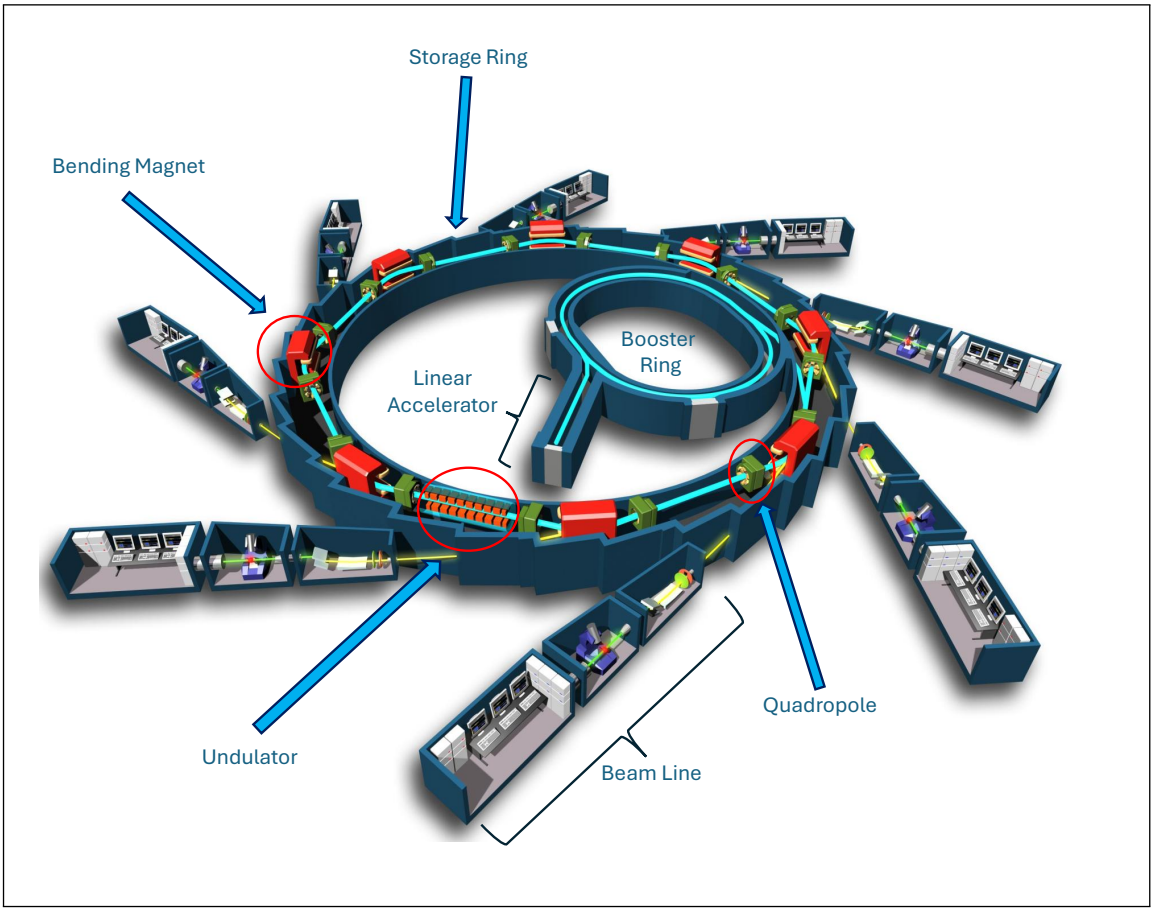

Figure 3.1: Schematic illustration of a synchrotron facility. The electrons start at the linear accelerator, before gaining further energy at the booster ring, before circulating the storage ring. Bending magnets, quadropoles and undulators are needed to obtain synchrotron radiation, which can be used for different experiments at the beam lines, such as powder X-ray diffraction. From EPSIM 3D/JF Santarelli, Synchrotron Soleil, Attribution, via Wikimedia Commons [34].

Figure 3.1 shows a schematics illustration of a synchrotron facility. In such a facility, electrons are first accelerated by a linear accelerator, followed by further increase

of their energy in the smaller booster ring, before being sent to the storage ring [35]. In the storage ring, the path of the electrons is directed and adjusted using bending magnets (diopoles), and kept confined using sextupoles and quadropoles. When passing the undulators, which consists of a series of bending magnets, the acceleration this forces on the electrons give rise to high intensity synchrotron radiation [35]. The interplay between magnets and the electrons as they are accelerated in the ring requires careful synchronisation, which is what gives the synchrotron its name [36]. In the beam lines can then different types of electromagnetic radiation be used to perform experiments, for example powder X-ray diffraction.

3.3 Powder X-ray Diffraction

Powder X-ray diffraction (PXRD) provides a method to determine the crystal structures present in a crystalline powder sample [37]. This is done by directing X-rays onto the powder sample, and studying the interaction between the electron cloud of the sample and the X-rays [38]. If the powder consists of tiny crystals, known as crystallites, then this will be a crystalline sample, where the crystal structure of the crystallites provides a long range periodical arrangement of atoms. This long range periodical arrangement of atoms leads to X-rays being scattered so that a large number of X-rays mutually reinforce each other in certain directions, while in other directions, the X-rays mutually cancel each other out - this is what is known as X-ray diffraction [1, 38]. X-rays mutually reinforcing each other are said to interact *constructively*, while X-rays cancelling each other out interact *destructively*. The directions in which X-rays are diffracted or not will depend on the angle between the incident X-rays and the crystallites in the powder. The result of this is that in directions where X-rays interact constructively, high intensities of X-rays can be detected, and in directions where they interact destructively, no noticeable (except background) intensities of X-rays are detected. The background intensity originates from diffuse X-ray scattering with air, or from imperfections in the crystallites, such as strain for example [38].

A schematic illustration of the result from a PXRD measurement, called a diffractogram, is shown in Figure 3.2. The 2θ-angle corresponds to the angle between the incident X-rays and the diffracted X-rays, see Figure 3.3. Each position where intensities of X-rays occur correspond to a specific plane in the unit cell, and is denoted by its Miller-indices (hkl). The positions where X-ray intensities show up can thus be called an hkl-reflection. The diffractogram looks the way it does based on the specific crystal structure(s) being examined. More specifically, the type and size of the unit cell determine the position of the hkl-reflections on the 2θ-axis, and the intensity of the hkl-reflections is determined by the type of atoms, and their position in the unit cell [38].

Different types of unit cells have different allowed hkl-reflections, that is, for a certain crystal structure, only certain combinations of the values on the h, k and ls result in X-rays interacting constructively [1]. Which hkl-values that give rise to an allowed reflection depending on a specific crystal structure can be derived from Equation (3.1).

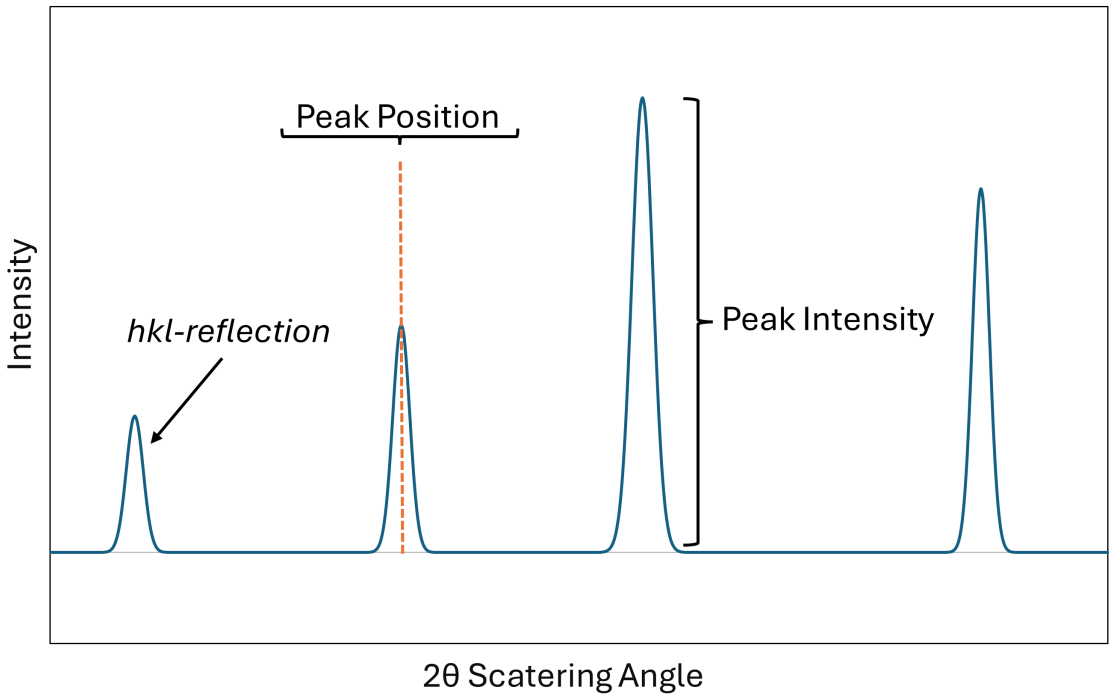

Figure 3.2: Schematic illustration of an X-ray diffractogram, showing how the intensity (y-axis) and position of the *hkl*-reflections vary with the diffraction angle 2θ (x-axis).

The intensities of the *hkl*-reflections, as those in Figure 3.2, are more specifically described by the sample's structure factor, F_{hkl} [39]. From the structure factor can it be seen that the intensities depend on the position of the atoms within the unit cell, how much they deviate (vibrate) from their equilibrium position, and how effectively they scatter X-rays. The structure factor can be expressed as

$$F_{hkl} = \sum_i t_i f_i e^{2\pi i(hx_i + ky_i + lz_i)}, \tag{3.1}$$

where we sum over the i number of atoms in a unit cell. The amount a specific atom deviates from its equilibrium position due to thermal vibration is described by t_i, and f_i describes how effectively a specific atom scatters X-rays[1]. The position of the atoms in the unit cell is given by coordinates x_i, y_i, z_i and the h, k and l refer to a specific *hkl*-reflection. The more an atom vibrates, described by t_i, the lower the intensity of an *hkl*-reflection is, since this spreads out the intensity over a wider 2θ-range [39].

The strength of the X-ray intensities is proportional to the square of the absolute value of the structure factor [39],

$$I_{hkl} \propto |F_{hkl}|^2. \tag{3.2}$$

[1]Known as the atomic scattering factor [1].

Several factors show up in the proportionality between the intensity and the structure factor, such as a Lorentz factor and a polarisation factor [39]. These are usually collectively referred to as an LP-factor, and describes the geometry of the diffraction measurement. There is also an overall scale factor present in the proportionality between the intensity and structure factor.

The conditions needed for X-ray diffraction in crystals to occur, that is, when we have X-rays interacting constructively, is given by the Bragg equation

$$n\lambda = 2\,d\,sin\,\theta. \tag{3.3}$$

Equation (3.3), also known as Bragg's law, relates the wavelength of the incident X-rays λ, to the distance between crystal planes d and the angle between the incident X-rays and the crystal planes θ. The integer n represents the order of diffraction, and describes rays scattered by neighbouring planes, namely how many wavelengths that are present in their path difference [38]. A derivation of the Bragg law can be found in for example *Elements of X-ray diffraction* by B.D. Cullity et. al [38].

Bragg's law makes it possible to determine the inter-planar spacing, d, by having a known angle θ and wavelength λ. Looking at a first order diffraction, $n = 1$, we get

$$d = \frac{\lambda}{2\,sin\,\theta}. \tag{3.4}$$

If we consider a cubic crystal system as an example, the lattice parameter a can be determined using Bragg's law and the cubic inter-planar spacing equation,

$$\frac{1}{d^2} = \frac{(h^2 + k^2 + l^2)}{a^2}, \tag{3.5}$$

where h, k and l are the Miller indices of an allowed reflection, and a the lattice parameter (the length of one side in the unit cell).

Rearranging this equation and combining it with Bragg's law yields

$$\frac{\lambda^2}{4\,sin^2(\theta)} = \frac{a^2}{(h^2 + k^2 + l^2)}, \tag{3.6}$$

resulting in the lattice parameter a being expressed as

$$a = \frac{\lambda\sqrt{(h^2 + k^2 + l^2)}}{2\,sin(\theta)}. \tag{3.7}$$

The lattice parameter a, can thus be determined from the hkl-values, in combination with knowing the wavelength of the X-rays and the angle θ.

Equation (3.7) also provides an example[2] of how the angle θ is related to a specific unit cell (different unit cells determines the allowed value of the sum $h^2 + k^2 + l^2$ due the selection rules) and its size (a in this case). This highlights the fact that the position of the hkl-reflections (the 2θ-angle) is determined by the type of unit cell and its size.

Figure 3.3 shows schematically how X-rays can be represented as being diffracted against crystallographic planes.

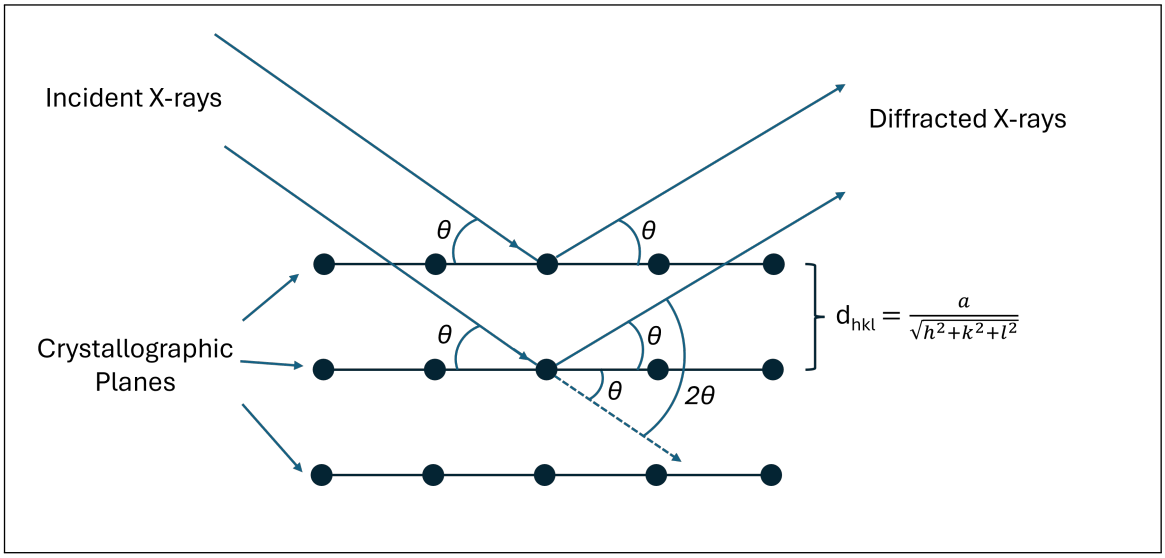

Figure 3.3: Schematic representation of how X-rays are diffracted by crystallographic planes depending on the incident angle θ. The interplanar spacing, d_{hkl}, refers to cubic crystal structures, and 2θ is the total scattering angle between the incident and diffracted X-rays. The black discs represent atoms in a crystal structure.

To summarise, the basis for determining crystal structures from PXRD-data stems from the fact that a crystal structure corresponds to a specific unit cell and the positions of the atoms within this unit cell. This information is precisely what a powder diffractogram provides via the intensities of the hkl-reflections and their position [38].

It is however not always possible to directly determine a sample's crystal structure from its powder diffraction data, due to reasons such as imperfections in the crystallites. The remainder of this section will be devoted to the limitations of the information contained in a PXRD diffractogram.

One of the limitations with powder X-ray diffraction arises from the fact that diffraction peaks can overlap. This is as a consequence of the diffractogram representing three-dimensional information (the crystal structure) on a one-dimensional axis (the 2θ-range) [40]. For instance, if two diffraction peaks have a very similar 2θ-value, they might overlap, and if there are several crystal phases present in a sample, their

[2]Different relationship between the lattice parameters, hkl-values, and inter planar spacing d applies to different crystal structures [1].

peaks might overlap as well. Moreover, in PXRD, peaks are subjected to broadening. Ideally, perfect crystals would mean that each hkl-reflection only happens at a single spot, resulting in sharp intensity peaks in the form of delta functions [38]. However, due to imperfections among the crystallites, peak intensities gets "smeared out" over a wider 2θ-range, compared to the ideal theoretical case, resulting in broadening of the diffraction peaks. Several factors give rise to the broadening of the hkl-reflections, two important being the size of the crystallites, and crystallite strain [38].

The influence of crystallite size on peak broadening is a result of small crystals lacking planes needed for destructive interference to occur [38]. This means X-ray intensity can be detected at 2θ-values which are close to the ideal value, leading to broadening of the diffraction peaks [38]. The effect of peak broadening due to small crystallite size is usually noticeable for crystallites smaller than 0.1 µm.

Scherrer's equation can be used to estimate the influence of crystallite size on peak broadening [41]

$$D = \frac{K\lambda}{\beta cos(\theta)}, \tag{3.8}$$

with D being the crystallite size, K a dimensionless constant determined by the size distribution and shape of the crystallites, λ and θ the wavelength of the X-rays and scattering angle respectively, and β the full width at half maximum (FWHM) of the hkl-reflections. From Scherrer's equation can it be seen that as the size of the crystallites, D, gets smaller, the FWHM (the "broadening"), β, becomes bigger.

Microstrain imposed on crystallites, means that crystallographic planes are compressed or expanded, and leads to variations in the inter-planar spacing, d, and in turn shifts in the 2θ-value. At a high-level, this can be seen from Bragg's law, Equation (3.3), where a shift in the d-spacing between crystallographic planes leads to a shift in the 2θ-values determining the peak position [38]. An expanded inter-planar spacing d, results in diffraction peaks showing up at lower 2θ-values and vice versa. If a crystallite is exposed to non-uniform strain, that is, certain crystallographic planes are compressed, others expanded, and some are at the ideal inter-planar spacing, then this leads to broadening of the diffraction peak, as a result of intensity being shifted to both higher and lower 2θ-values [38]. The effect of uniform compression, uniform expansion and non-uniform strain of crystallographic planes is illustrated in Figure 3.4.

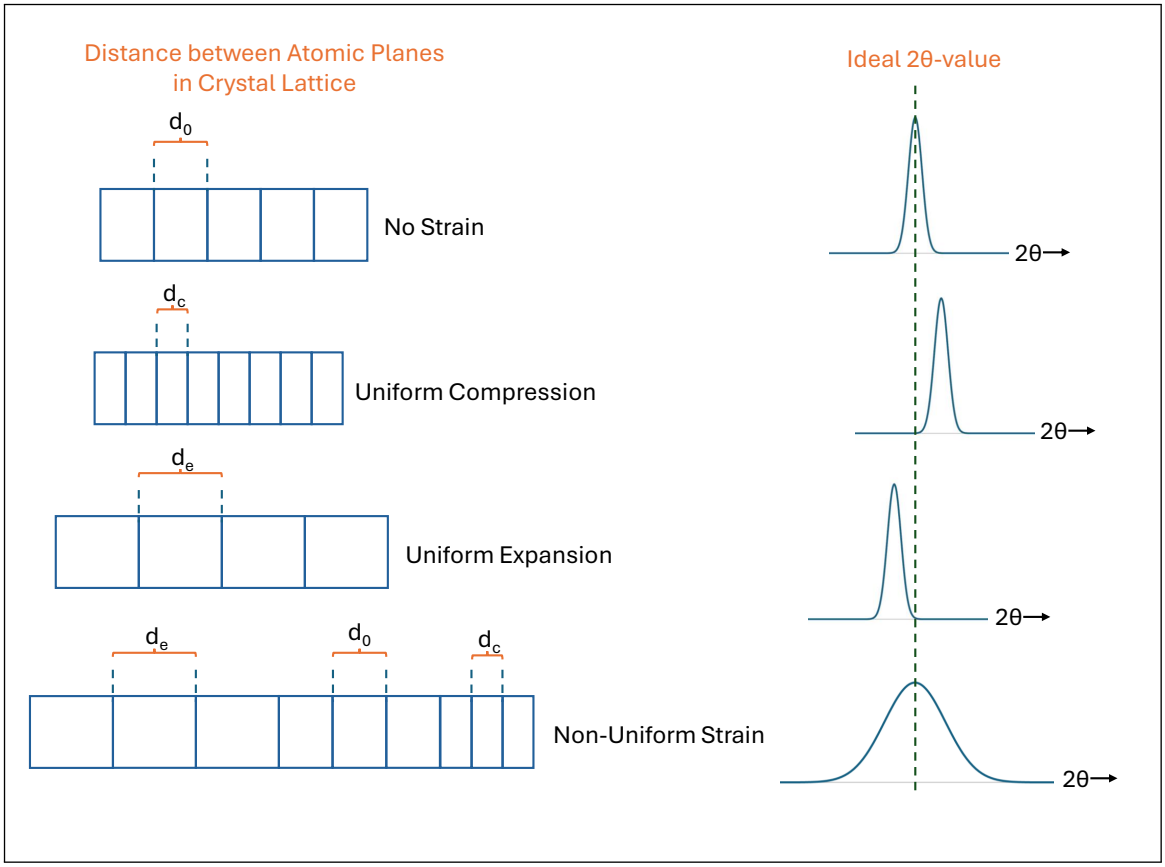

Figure 3.4: Illustration of how different types of strain affect peak position and broadening. The ideal spacing between planes is referred to as d_0. Compression of crystal planes, d_c, results in shifting hkl-reflections to larger 2θ-values. Conversely, expansion of crystal planes, d_e, causes the hkl-reflections to shift to lower 2θ-values. Non-uniform strain occurs if we have a crystal with both expansion, compression and the ideal spacing present, which causes the hkl-reflections to be broadened.

A method used for determining the crystal structure in a powder sample, which tackles the problem with peak overlap and broadening, is the *Rietveld refinement* method, which will be given a brief introduction in the nest section.

3.4 Rietveld Refinement

First introduced by Dutch crystallographer Hugo Rietveld in the 1960s [42], at its core, the Rietveld refinement method is a way of calculating crystal structures present in a sample from its powder diffraction data.

This is done by comparing the observed diffraction intensities with calculated intensities [40]. The calculated intensities depend on a set of adjustable parameters, and when the observed and calculated intensities are as close to each other as possible in a least squared fashion, the parameters are said to be refined. This is expressed by Equation (3.9),

$$\sum_i (y_{\text{obs},i} - y_{\text{calc},i})^2 \rightarrow \{\text{Varying Parameters}\} \rightarrow \text{Min}, \tag{3.9}$$

where $y_{\text{obs},i}$ and $y_{\text{calc},i}$ are the observed and calculated intensities at position i in the 2θ-range in a PXRD diffractogram.

The parameters used in the Rietveld refinement capture various physical origins of why a diffractogram look the way it does, and this depends on both the instrument and sample [40]. A brief introduction to some of the parameters used during a Rietveld refinement will be given below. For a more elaborate discussion, the reader may look into *Rietveld Refinement Practical Powder Diffraction Pattern Analysis using TOPAS* by Robert E. Dinnebier et al. [40]. Additionally, methods for modelling the background intensity, how the mass fraction of a crystalline phase is estimated, the quality of a refinement and the complementary Pawley whole-pattern-fitting method will be discussed.

3.4.1 Peak Position

The position of the *hkl*-reflections depends on the allowed *hkl*-reflections, and thus which symmetry space group that is used during the refinement. Their position also depends on, and is modelled with, instrumental factors such as the sample displacement and zero-error [40]. Zero-error being deviations in the instrument set-up from the true 2θ zero-point [39].

3.4.2 Peak Intensity

The intensity of the *hkl*-reflections depends on the structure factor[3], Equation (3.1),

$$F_{hkl} = \sum_i t_i f_i e^{2\pi i(hx_i + ky_i + lz_i)}, \tag{3.1}$$

which in turn depends on the atomic positions x_i, y_i, z_i. The position of the atoms, and to the extent which a site is occupied (the occupancy), thus becomes parameters to refine, in order to calculate the correct observed PXRD intensity in a measurement.

As discussed in Section 3.3, the intensity also depends on how much the atoms vibrate due to available thermal energy, making a temperature factor another refinable parameter. If the atoms are assumed to move equally in all directions, this can be described isotropically by the atomic displacement factor B, which determines the t_j factor in Equation (3.1), according to

$$t_j = e^{-B\left(\frac{sin\theta}{\lambda}\right)^2}, \tag{3.10}$$

[3] As seen in Equation (3.2).

where θ is half the diffraction angle and λ the wavelength of the X-rays. The displacement factor B is also referred to as the Debye-Waller factor or temperature factor [39], and it is defined as the root mean square of the atomic displacement from its equilibrium position, u [39, 40],

$$B = 8\pi^2 u^2. \tag{3.11}$$

With u being given in Ångström (Å), B is thus reported in Å^2, and for inorganic samples, B-values between 0.1 Å^2 to 1.5 Å^2 are usually considered normal [40]. Larger values than 1.5 Å^2 can indicate disorder in the atomic arrangement or errors in the calculated crystal structure [40].

3.4.3 Peak Shape

Two factors affecting the shape of the intensity peaks are the size of the crystallites and strain imposed on the crystallographic planes (microstrain, see Figure 3.4), since these factors leads to broadening of diffraction peaks, as discussed in Section 3.3.

There exist different methods to model the shape of the peaks in X-ray diffractograms. One common method is by using a convolution between a Gaussian distribution, $G(x)$, and Lorentzian distribution, $L(x)$, called a Voigt distribution, $V(x)$ [40],

$$V(x) = G(x) \circ L(x). \tag{3.12}$$

A somewhat simpler version of the Voigt distribution is the pseudo-Voigt distribution, $pV(x)$. This is a linear combination of a Gaussian and Lorentzian distribution instead of a convolution,

$$pV(x) = \eta G(x) + (1 - \eta)L(x), \tag{3.13}$$

where η goes between 0 to 1 [43]. Figure 3.5 (a) shows a Gaussian and Lorentzian distributions, and (b) compares a pseudo-Voigt distribution to the Gaussian and Lorentzian distributions.

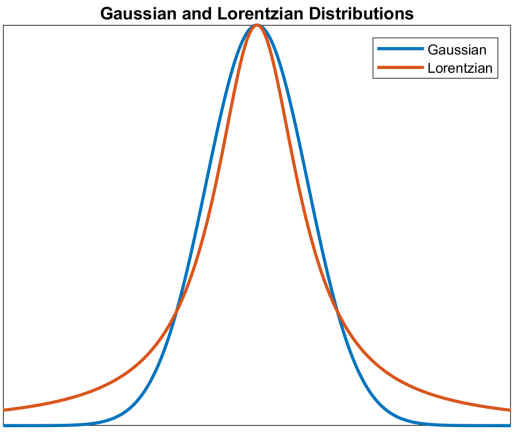

((a))

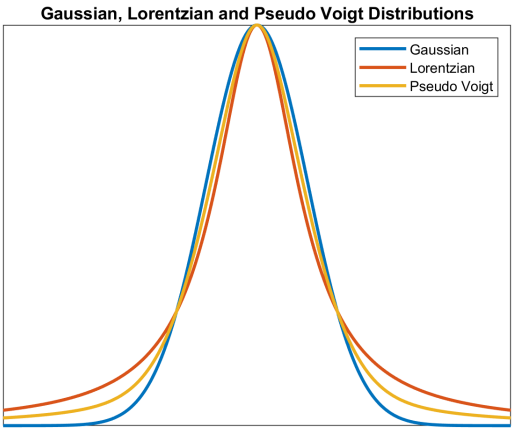

((b))

Figure 3.5: Illustration showing the difference between a Gaussian and Lorentzian (also called Cauchy) distribution in (a). (b) shows the Pseudo Voigt distribution for $\eta = 0.5$, and how it compares to the Gaussian and Lorentzian distribution.

3.4.4 Background Intensity

The background intensity in a diffractogram is typically modelled using first kind Chebyshev polynomials of order 5-15 [40]. It is important to note, however, that the higher the order of Chebyshev polynomial used, the higher will the correlation be between the intensity of overlapping hkl-reflections at larger 2θ-values and the background coefficients.

3.4.5 Quantitative Phase Analysis

If a PXRD sample is assumed to consist entirely of crystalline phases, and these phases are identified, then can the weight fraction of phase p, W_p, be expressed in terms of the unit cell volume V_p, number of formula units per unit cell Z_p, the mass of the formula unit M_p, and the scale factor S_p [44]. The mass of a crystalline phase, m_p, can be expressed using the above mentioned entities according to

$$m_p = S_p Z_p M_p V_p C = S_p (ZMV)_p C, \tag{3.14}$$

where C is a constant originating from the specific PXRD measurement, capturing effects from the instrument calibration and sample absorption coefficient [44, 45]. Since the weight fractions sum to one under the assumption that a sample solely consists of identified crystalline phases, the weight fraction, W_p, can be expressed as

$$W_p = \frac{S_p (ZMV)_p}{\sum_{i=1}^{n} S_i (ZMV)_i}, \tag{3.15}$$

where the measurement specific constant C is cancelled out.

3.4.6 Quality of a Refinement

The quality of a refinement can be evaluated by comparing the weighted difference between the observed and calculated pattern to a weighted observed pattern, as done by the weighted Residual-index, or R_{wp}-value [43, 1],

$$R_{wp} = \sqrt{\frac{\sum_i w_i (y_{\text{obs},i} - y_{\text{calc},i})^2}{\sum_i w_i (y_{\text{obs},i})^2}}. \tag{3.16}$$

In Equation (3.16), the weight is calculated as $w_i = \frac{1}{\sigma(y_{\text{obs},i})}$, $\sigma(y_{\text{obs},i})$ being the experimental uncertainty of the observed intensity [39].

The R_{wp}-value can in turn be compared to the statistically expected R-value, R_{exp}, defined as

$$R_{exp} = \sqrt{\left(\frac{(N-P)}{\sum_i w_i (y_{\text{obs},i})^2}\right)}, \tag{3.17}$$

where N is the number of data points from the diffraction measurement, and P the number of refined parameters [43].

Taking the ratio between R_{wp} and R_{exp} gives us the "Goodness of Fit" (GoF) measure for a refinement,

$$\text{GoF} = \frac{R_{wp}}{R_{exp}} = \sqrt{\frac{w_i \sum_i (y_{\text{obs},i} - y_{\text{calc},i})^2}{N-P}}. \tag{3.18}$$

The goodness of fit value is also often denoted χ, and typically, a Rietveld refinement is considered to be "good" when the GoF is between 1 to 1.5 [40].

Even though the different R-values can be used to evaluate the quality of a refinement, the best way is usually a visual inspection of the difference between the observed and calculated intensities [43], which an example of can be seen in Figure 5.5.

3.4.7 Pawley Fit

Prior to performing a Rietveld refinement, a whole powder diffractogram fitting method may be used, which does not take into account structural aspects such as the atomic positions when calculating the intensities [40]. One such fitting method is the Pawley fit, which enables one to obtain parameters describing the background intensity, peak positions, and peak profiles of a sample. It is useful to have an estimate of these parameters prior to performing a Rietveld refinement, since it is

then possible at the start of a refinement to focus on how other structural aspects in the unit cell, such as the occupancy and atomic positions, influences the intensities. Additionally, the Pawley fit gives an indication of the best weighted profile R-value, R_{wp}, possible to achieve for a given measurement [40].

Although PXRD in combination with Rietveld refinement is a powerful method for determining crystal structures, one limitation is the difficulty to detect elements which are weak X–ray scatterers, that is, when the atomic scattering factor f_i in Equation (3.1)

$$F_{hkl} = \sum_i t_i f_i e^{2\pi i(hx_i+ky_i+lz_i)}, \tag{3.1}$$

is very small. One example of an element with a small atomic scattering factor is hydrogen, making it virtually non-detectable using X-ray diffraction [38]. A complementary technique to powder X-ray diffraction for characterising materials, which can be used to investigate the presence of hydrogen bonds, is infrared spectroscopy, which will be discussed in the following section.

3.5 Infrared Spectroscopy

The fact that molecules can absorb certain frequencies of infrared (IR) light as vibrational motion, which will be characteristic to a specific molecular structures, is exploited in infrared spectroscopy [46]. By measuring the transmittance or absorbance of a sample for different frequencies of infrared light, an infrared spectrum can be attained, usually reported in transmittance or absorbance versus wavenumber, cm^{-1} (number of wavelengths per centimetre).

Today, for practical measurement, infrared spectroscopy is mostly utilized in the form of Fourier transform infrared spectroscopy (FTIR) [46]. Using FTIR means that instead of measuring the absorption/transmittance of each infrared frequency individually, as in traditional dispersive infrared spectroscopy, the whole frequency range investigated can be measured at the same time.

To perform FTIR, a Michelson interferometer can be used, which consists of an IR light source, a beam splitter, and two mirrors, one fixed and one moveable [46]. Figure 3.6 shows a schematic sketch of the set-up. In the Michelson interferometer, IR-light from the source is directed to both the fixed and moveable mirror by the beam splitter, and as the two beams of IR-light recombine at the beam splitter (after being reflected by the mirrors), they will interfere with each other. Since the position of the moveable mirror is altered, this creates a path difference for the two beams of IR-light. The path difference in turn introduces a phase difference for the different frequencies of IR-light, leading to the two beams interfering in different ways depending on the position of the moveable mirror. This creates an interference pattern as a function of mirror position, called an interferogram [46]. After the recombined beam's intensity has changed as a consequence of interacting with the sample, the beam reaches the detector, where an interferogram signal versus

mirror position is registered. The Fourier transform is then applied to go from the interferogram, which varies with time (depending on the mirror position), to a more easily interpretable transmittance/absorption versus frequency (wavenumber) signal [46].

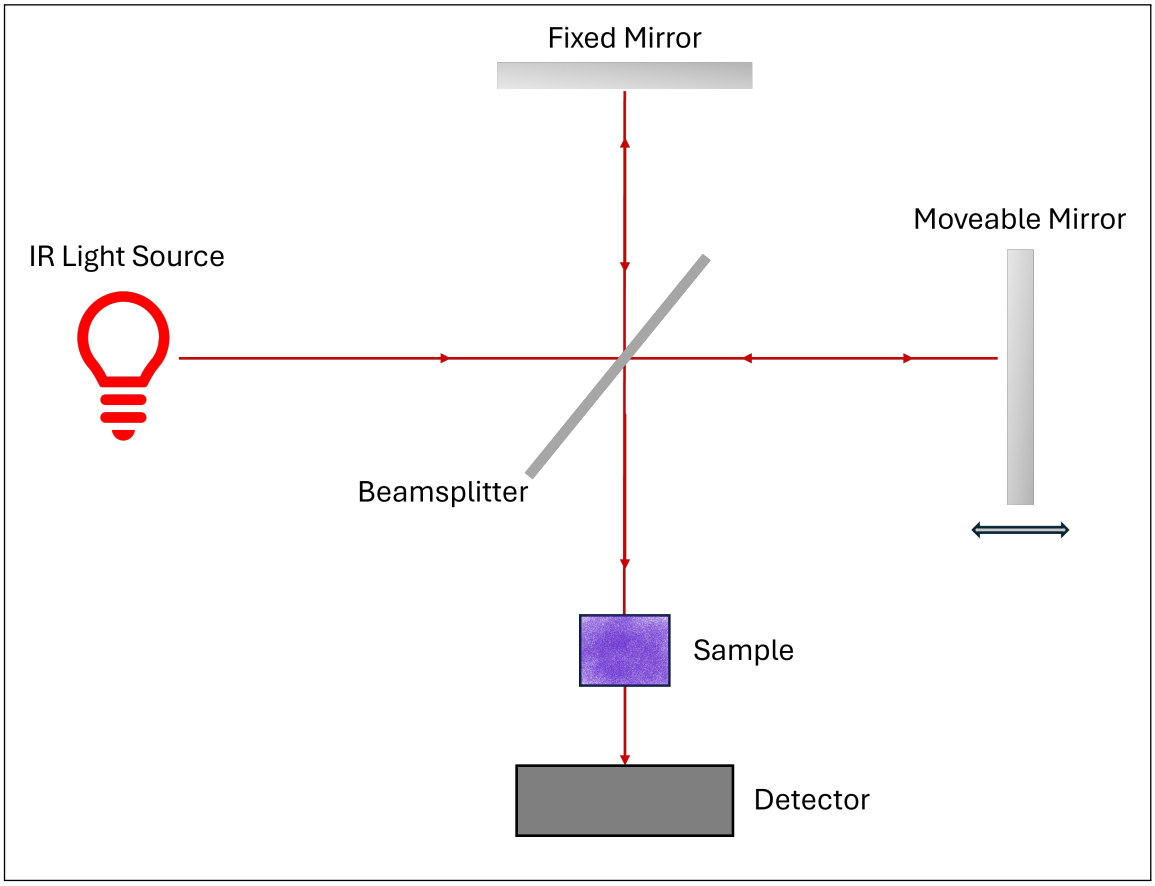

Figure 3.6: Illustration of a Michelson Interferometer. The IR-light from the source is directed to both the moveable and fixed mirror by the beamsplitter. After being reflected, the IR light from the fixed and moveable mirror is recombined at the beam splitter, and the recombined beam then interacts with the sample, before being registered by the detector.

There are different ways to perform Fourier transform infrared spectroscopy measurements, one suitable for powders being *Attenuated Total Reflectance* (ATR) [46]. This method uses a crystal with a high refractive index (typically zinc-selenide, germanium or diamond) which is in contact with the sample being investigated [47]. When infrared light passes through this crystal at a high angle (higher than a specific critical angle), total internal reflection will occur at the boundary of the crystal-sample interface [47]. An evanescent wave will then be created at this interface, reaching typically a couple of micrometres into the sample. The intensity of the reflected evanescent wave will be reduced if the sample is IR-active, which is registered by the detector. A schematic sketch of an attenuated total reflectance set up is given below in Figure 3.7.

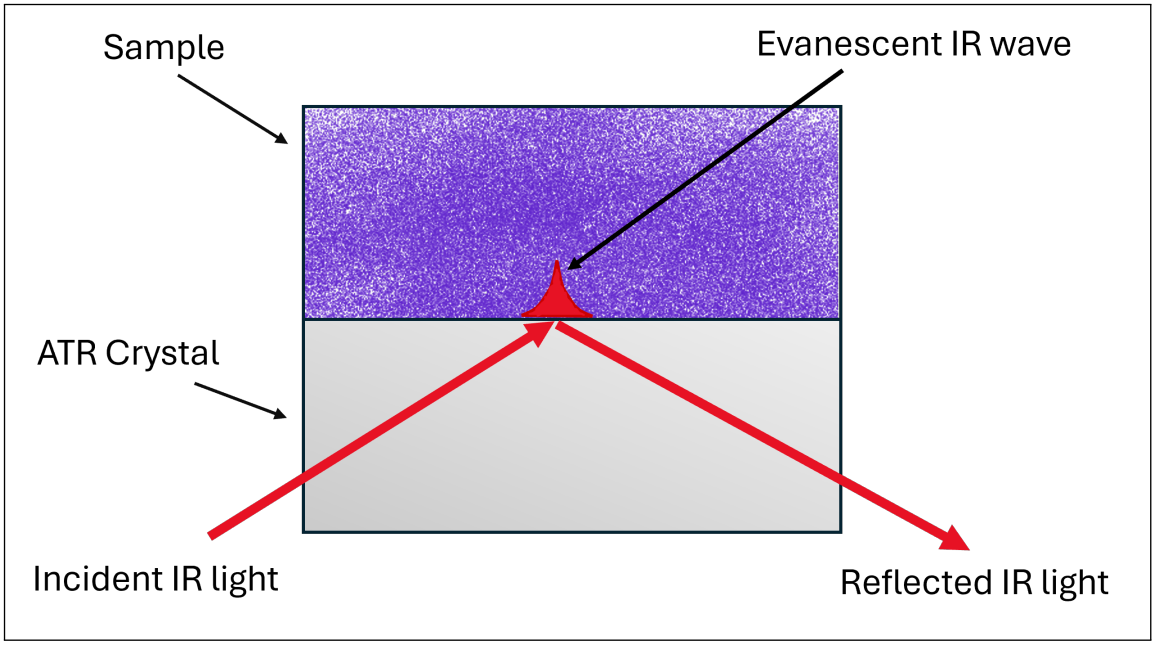

Figure 3.7: Illustration of an attenuated total reflectance interaction, showing one reflection. Total internal reflection occurs at the crystal-sample interface, resulting in an evanescent IR wave being created in the sample. The reflected IR-light will have a reduced intensity if the sample is IR active.

Chapter 4

Experimental

The details of the different experimental procedures used in this project are provided in this chapter. The samples have been synthesised at Chalmers University of Technology, and Chalmers Material Analysis Laboratory (CMAL) facilities have been used for the characterisation, with the exception for the synchrotron measurements.

4.1 Synthesis

Copper doped strontium apatite was synthesised using a series of heating steps, with intermittent re-grindings. A detailed description of the main synthesis employed, synthesis method 1, is as follows, and is also summarised in Figure 4.1.

Strontium carbonate ($SrCO_3$, Merck), ammonium dihydrogen phosphate ($(NH_4)H_2PO_4$, Scharlau > 99 %) and copper (II) oxide (CuO, Acros Organics > 99 %) were mixed in molar ratios of 5.05 : 3 : 1 ($SrCO_3$: $(NH_4)H_2PO_4$: CuO), and ground using mortar pestle and propan-2-ol (isopropanol, IPA). The IPA was let to evaporate in an 80 °C drying cabinet. The sample was then heated in a muffle furnace from room temperature to 400 °C at 600 °C/h, and dwelled for 2 hours at 400 °C, followed by cool down to room temperature inside the furnace.

The powder was then ground, ball milled and pressed into pellets. The pellets were heated from room temperature to 700 °C at 300 °C/h, followed by dwelling at 700 °C for 2.5 hours and cool down to 30 °C at 300 °C/hour.

The pellets were again ground, ball milled and pressed into pellets before being annealed, by heating from room temperature to 1100 °C at 300 C/h, followed by 24 hours of dwelling and air quenching.

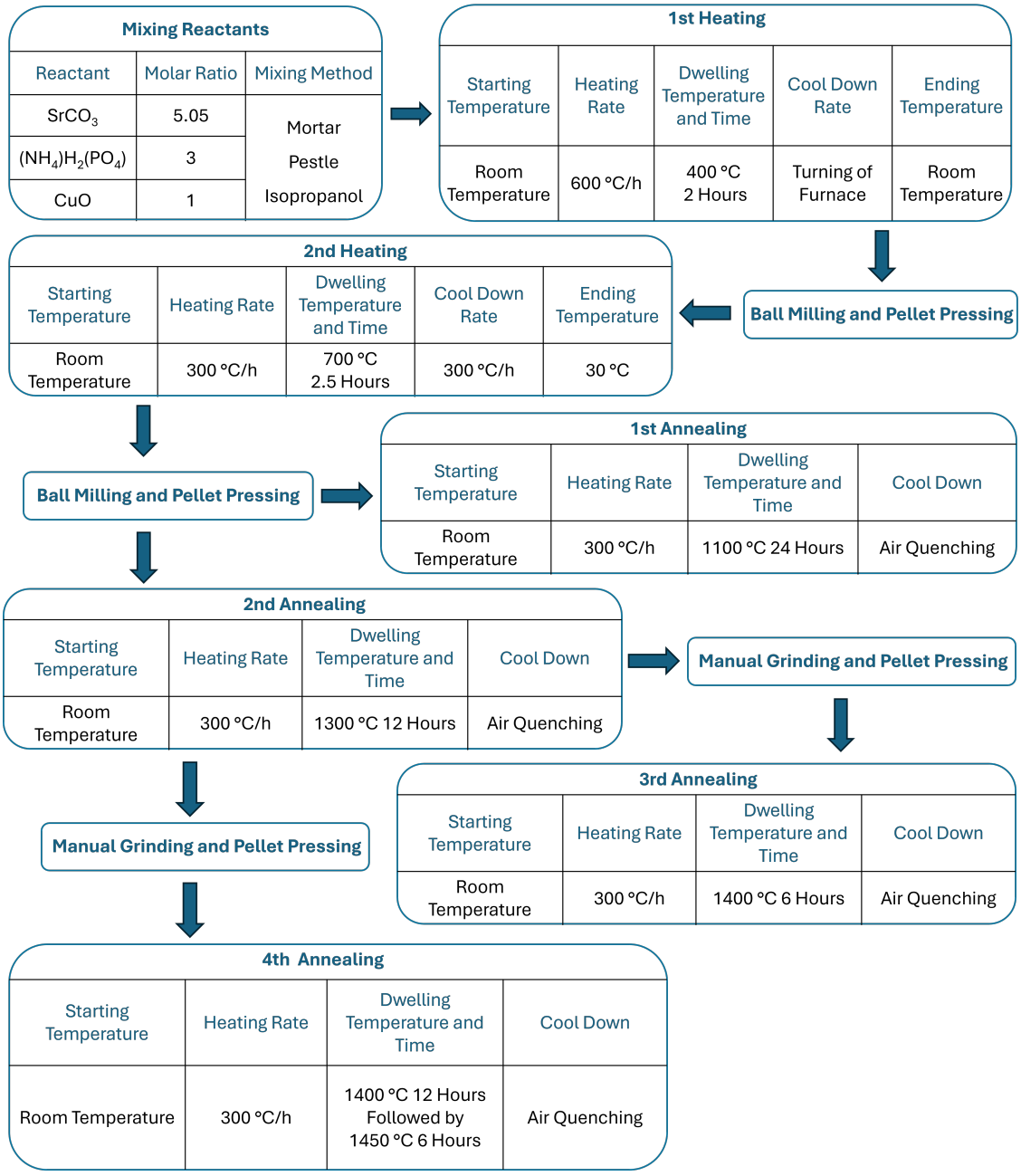

Figure 4.1: Flowchart summarising the different steps in synthesis method 1. Manual grinding refers to mixing using mortar, pestle and IPA.

Apart from annealing at 1100 °C, additional annealing temperatures and times which have been evaluated are 1300 °C 12 h (annealing with 700 °C sample), 1400 °C 6 h (annealing with 1300 °C sample), and 1400 °C 12 h + 1450 °C 6 h in one session (annealing with 1300 °C sample). All samples were ground and mixed using mortar, pestle and isopropanol and pressed into pellets before being annealed in a tube furnace. The heating rate used was 300 °C/h.

It was also tested to heat a sample previously annealed at 1100 °C, to 1500 °C for 5 h followed by air quenching, which resulted in a melt. Once this was discovered,

it was tested to melt a sample at 1500 °C and cooling it down slowly, to see if this could work as a method for synthesising single crystals. This was done on a sample previously annealed at 1450 °C, heating it from room temperature to 1500 °C at 250 °C/h, followed by 1 hour of dwelling, and then slowly cooling it down to 1450 °C at 5 °C/h. This procedure was done in a platinum crucible instead of an alumina boat.

4.1.1 IR Samples

Due the lack of sample substance, another batch was synthesised for the IR-spectroscopy measurements. This synthesis followed a similar, but slightly adjusted pathway compared to synthesis method 1, and will be referred to as synthesis method 2. In order to save time, less intermediate re-grindings were performed, and ball-milling was not utilized. The same molar ratios between $SrCO_3$ (Merck), $(NH_4)H_2PO_4$ (Scharlau, > 99 %) and CuO (Acros Organics, > 99 %) were used as in synthesis method 1. However, instead of heating the reactants in several pre-annealing sessions, one session was used comprising of 400 °C 2 h dwelling, 600 °C 1 h dwelling, and 850 °C 10 h dwelling, and then cool down to 30 °C. The heating rate used was 300 °C/h.

Annealing was performed by heating pelletised samples at a rate of 300 °C/h from room temperature to 1150 °C 24 h, 1400 °C 6 h and 1450 °C 4 h. All annealing was performed in a tube furnace, and terminated by air quenching. In between the different annealing sessions, samples were ground using mortar, pestle and IPA, and pressed into pellets.

Figure 4.2 provides a flowchart summarising synthesis method 2.

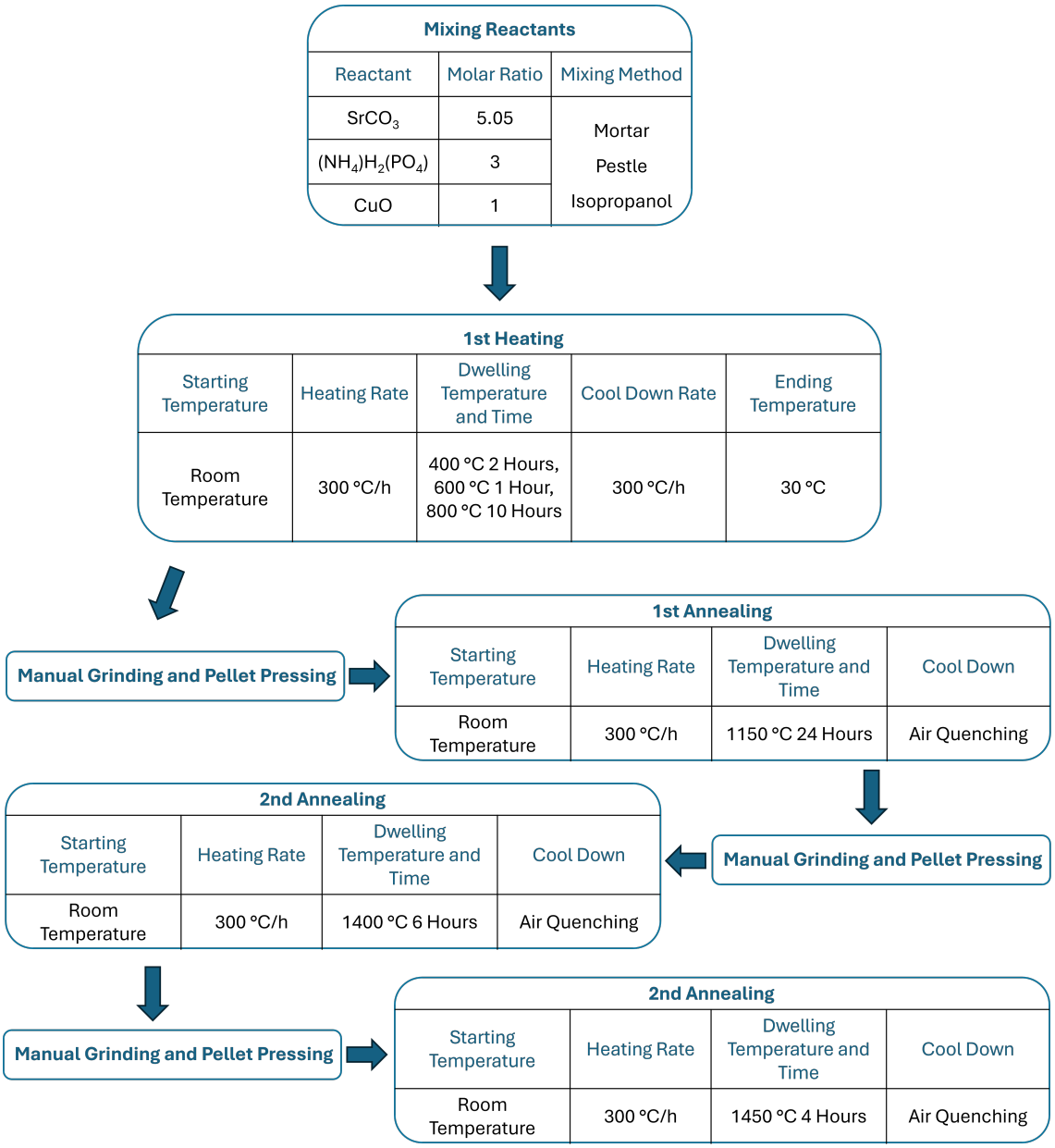

Figure 4.2: Flowchart summarising the different steps in synthesis method 2. Manual grinding refers to mixing using mortar, pestle and IPA.

4.2 Analysis

In this section will the different methods used for analysing the synthesised materials be reviewed, that is, the, synchrotron PXRD, Rietveld refinement and infrared spectroscopy measurements.

4.2.1 Synchrotron PXRD

Synchrotron measurements on samples made with synthesis method 1 were performed at the Diamond Light Source in the United Kingdom, using a Debye-Scherrer transmission geometry and operating with X-rays of 0.494 Å. The 2θ-values ranged from 2.10 to 69.23 degrees.

Synchrotron measurements of samples made with synthesis method 2 were performed by Momentum Transfer at the European Synchrotron Radiation Facility (ESRF), using a Debye-Scherrer transmission geometry and operating with X-rays of 0.16520 Å. The 2θ-values ranged from 0.6 to 13.5 degrees.

4.2.2 Rietveld Refinement

The Rietveld refinements of the obtained synchrotron PXRD data was performed using the TOtal Pattern Analysis Solution (TOPAS) version 6 [48]. Crystallographic information files (CIF) for copper-doped strontium apatite ($Sr_5(PO_4)_3(CuO_2)_{1/3}$) and strontium phosphate ($Sr_3(PO_4)_2$) have been used as structures to base the refinement on [49, 50]. These crystallographic phases were selected since they have been reported to be present when performing a similar synthesis [27]. There were also no other noticeable diffraction peaks not covered by the $Sr_5(PO_4)_3(CuO_2)_{1/3}$ and $Sr_3(PO_4)_2$ phases. During the Rietveld refinements, parameters were released and fixed following the suggested pathway from Dinnebier et al. in Ref. [40]. The 2θ-range investigated for the samples made with synthesis method 1 was 3-42, to include the first hkl-reflection observed at 3 degrees, and since no noticeable intensity except background were observed after 42 degrees. The 2θ-range for the IR sample made with synthesis method 2 investigated was 0.6-13.5 degrees.

A standard refinement started with performing a Pawley fit, first refining lattice parameters and the background (10 term Chebyshev polynomial). Following this was the zero-error and a cylindrical 2θ-correction for peak position adjusted. Finally, were the Gaussian and Lorentzian contributions from microstrain and crystallite size on the peak profile refined.

Refined parameters from the Pawley fit were transferred to the Rietveld refinement and initially held fixed.

The Rietveld refinements started with adjusting the scale factor and intensity correction, followed by atomic coordinates, except symmetrically important coordinates, such as e.g. a (0, 0, 1/4)-position. An overall isotropic atomic displacement parameter was then introduced for the atoms in each phase.

The background and peak profile were again refined, followed by individual isotropic displacement parameters for the different atoms, and the occupancy of the Cu- and O4-sites (see Figure 5.6) in the $Sr_5(PO_4)_3(CuO_2)_{1/3}$ - phase.

At the end, all previous refined parameters were released at the same time.

For the sample made with synthesis method 2, the refinement was made on a background subtracted- and angular offset corrected file, and peak-broadening due to microstrain was modelled using the Stephens approach [51].

4.2.3 Infrared Spectroscopy

The infrared spectroscopy measurements were performed at CMAL, utilizing a Bruker Vertex70v spectrometer, measuring with infrared light between 350 cm^{-1} to 4000 cm^{-1}. Prior to the sample measurements, a measurement on the surrounding air was performed as a reference for subtraction of background contribution. The measurements were performed in an attenuated total reflectance (ATR) set-up, using a diamond crystal. IR spectroscopy was performed on sample made with synthesis method 2, annealed at 1150, 1400, and 1450 °C. Other samples were not investigated due to lack of sample substance. IR-spectroscopy was mainly used to get a qualitative indication of whether or not there were OH-bonds present in the synthesised samples.

Chapter 5

Results & Discussion

In this chapter are first visual results from the synthesis presented in Section 5.1 and 5.2. The results from the synchrotron PXRD measurements and Rietveld refinements are provided in Section 5.3 and 5.4 respectively. Finally, in Section 5.5, are the IR-spectroscopy results presented.

5.1 Synthesis of Copper-Doped Strontium Apatite

During the pre-annealing steps of the synthesis, samples went from white to light grey in colour. However, after annealing at 1100 °C for 24 hours and air quenching, the colour changed from grey to purple. This is in rather well agreement with the blue-violet colour previously reported for single crystals of copper-doped strontium apatite synthesised using arc melting [27], and can be compared to strontium hydroxyapatite $Sr_5(PO_4)_3O_2H_{2-\delta}$, reported to be white in colour [28]. It can thus be suggested that the copper doping plays a key role in purple colour of copper-doped strontium apatite. It has also previously been shown that air quenching is required for copper-doped strontium apatites to acquire their colours, showing the necessity to use air quenching in order to obtain the wanted copper-doped strontium apatite phase [52]. The 1300 °C 12 h and 1400 °C 6 h samples were also purple, and an example of a pellet annealed at 1400 °C for 6 hours can be seen in Figure 5.1.

IR samples made with synthesis method 2 had the same characteristic purple colour as the samples from synthesis method 1.

Figure 5.1: Pellet after being annealed at 1400 °C for 6 hours and air quenched, demonstrating the purple colour it obtains.

5.2 Synthesis of Additional Phases

Since single crystals of copper-doped apatite have been reported to be synthesised at approximately 1600-1700 °C [27], it was tested to heat pellets from synthesis method 1 to 1500 °C for 5 h. However, this resulted in a melt. After cool down by air quenching, the sample heated to 1500 °C solidified into a glassy material. The melt adhered to the alumina boat in which it was contained, see Figure 5.2. The melting temperature is in rather well agreement with the melting temperature reported for single crystals of copper-doped strontium apatite, reported to be 1650 °C [27].

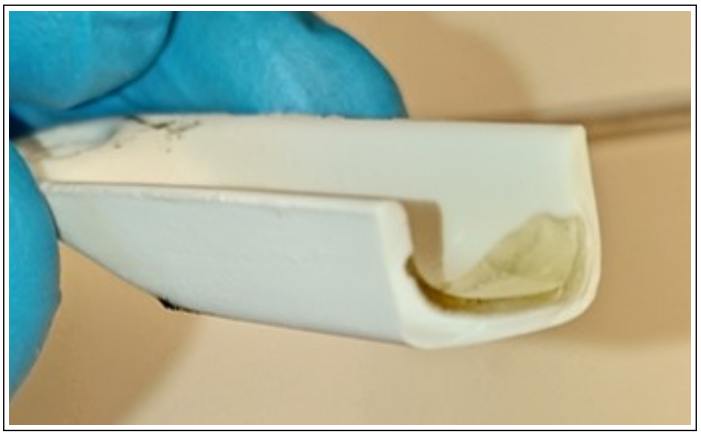

Figure 5.2: Melted pellet in an alumina boat after being heated at 1500 °C for 5 h. This procedure also had the side effect of breaking the alumina boat.

The result of heating a sample at 1500 °C for 1 h, and slowly cooling it to 1450 °C inside the furnace at 5 °C/h resulted in agglomerates of a purple-grey powdered material, see Figure 5.3. This was done in a platinum boat in order to avoid the sample adhering to the crucible it was heated in.

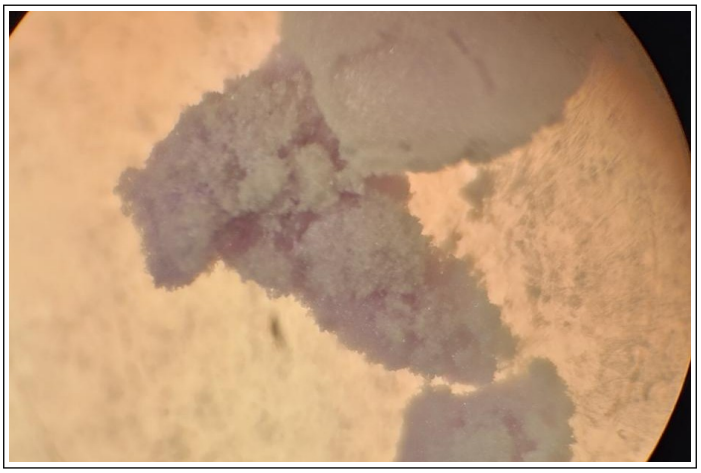

Figure 5.3: Optical microscope image of a sample heated at 1500 °C for 1 h, and then slowly cooled to 1450 °C at a 5 °C/h, before being air quenched.

5.3 Synchrotron PXRD

Figure 5.4 shows the synchrotron PXRD results of the samples made with synthesis method 1, annealed at 1100 °C 24 h, 1300 °C 12 h and 1400 °C 6 h respectively. One noticeable aspect is how the intensity of the two peaks, identified as the main peaks originating from the unwanted $Sr_3(PO_4)_2$ side phase, becomes lower as the annealing temperatures increases.

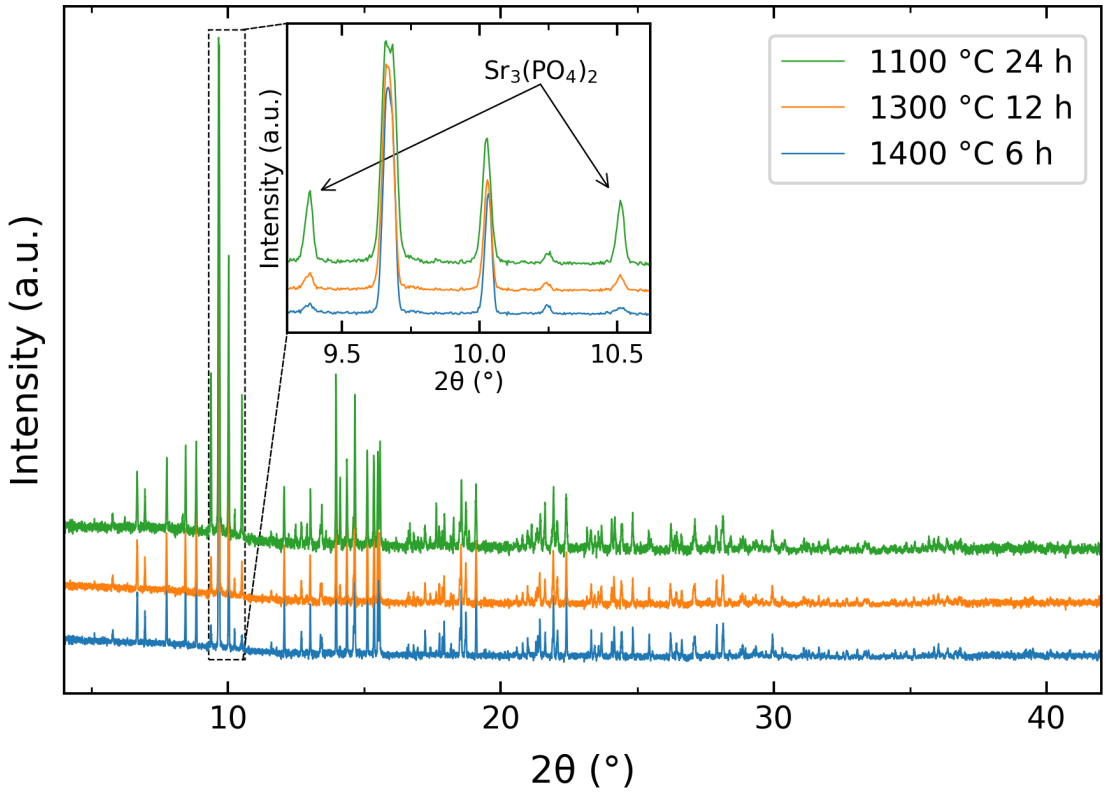

Figure 5.4: Results from the synchrotron PXRD measurements of the samples made with synthesis method 1, and annealed at 1100 °C 24 h, 1300 °C 12 h and 1400 °C 6 h respectively. The inset shows that the intensity of the two main $Sr_3(PO_4)_2$ peaks become lower at higher annealing temperatures.

5.4 Rietveld Refinement of PXRD Data

Table 5.1 summarises important compositional and structural results from the Rietveld refinement on synchrotron PXRD-data for the samples made with synthesis method 1. Note that 1400 °C was the annealing temperature which resulted in the highest mass fraction of the wanted $Sr_5(PO_4)_3(CuO_2)_{1/3}$ phase.

Table 5.1: Summary of the Rietveld refinements done on samples from synthesis method 1 and annealed at 1100 °C 24h, 1300 °C 12h and 1400 °C 6h respectively. The uncertainty in the calculated values (values in the parenthesis) is given as the calculated standard deviation from TOPAS, multiplied by a factor of three. Larger deviations are given in parenthesis using (± value). CuSrApt refers to the calculated copper-doped strontium apatite structure.

Summary of Rietveld Refinements from Synchrotron PXRD Data			
$Sr_5(PO_4)_3(CuO_2)_{1/3}$ Space Group	$P6_3/m$		
$Sr_3(PO_4)_2$ Space Group	$R\bar{3}m$		
Annealing Temp & Time	1100 °C 24h	1300 °C 12h	1400 °C 6h
R_{wp}	2.25	2.03	2.05
GoF	1.52	1.33	1.27
Site Occ. Cu	0.306(29)	0.317(23)	0.322(8)
Site Occ. O4	0.95(11)	0.993(96)	0.948(35)
B_{iso} Cu (Å^2)	1.04 (± 1.29)	0.38(87)	0.87(91)
B_{iso} O4 (Å^2)	1.78 (± 2.27)	2.79 (± 1.94)	4.50 (± 2.32)
d-Cu-O4 (Å)	1.822	1.825	1.825
Lattice Parameter a (Å) CuSrApt	9.7841(87)	9.7815(61)	9.7817(44)
Lattice Parameter c (Å) CuSrApt	7.2907(64)	7.3011(45)	7.3001(32)
Wt. % CuSrApt	81.41(92)	93.14(84)	96.02(76)
Wt. % $Sr_3(PO_4)_2$	18.59(92)	6.86(84)	3.98(76)

The lattice parameters stayed rather consistent for the different synthesis conditions with a being in the range 9.782-9.784 Å and c 7.291-7.301 Å. This can be compared to the lattice parameters for the non-Cu-doped strontium hydroxyapatite, $Sr_5(PO_4)_3OH$, where $a = 9.745$ och $b = 7.265$ [25]. Substituting of hydrogen ions for bigger copper ions in the one-dimensional channels thus suggests to result in somewhat larger lattice parameters for the for copper-doped strontium apatite versus strontium hydroxyapatite.

The distance between the copper and oxygen in the one-dimensional channels (see Figure 5.6), d-Cu-O4, was calculated to be 1.822-1.825 Å. This is in well agreement with the corresponding value from single crystals of $Sr_5(PO_4)_3(CuO_2)_{1/3}$ at 1.825 Å [27]. This value is also similar to the Cu-O bond length reported for $AlCuO_2$

and $FeCuO_2$, which have linearly coordinated Cu(I)-O bonds of 1.86 and 1.84 Å respectively [53, 54]. The calculated bond length of 1.825 Å thus potentially suggests that copper has oxidation state (I) in the samples made using synthesis method 1, due to the similar bond length in other linearly coordinated Cu(I)-O bonds. Note that for the calculated d-Cu-O4, the Cu-position along the c-axis, Cu_z, was not refined (see Table 5.2). Not refining the Cu_z-position results in the similar d-Cu-O4 between the calculated structures and the $Sr_5(PO_4)_3(CuO_2)_{1/3}$-structure the refinements was based on.

If the Cu_z-position is refined, it still converges towards zero at 0.00009, but with a substantial estimated standard deviation of ± 0.92 for the 1400 °C 6 h sample. Similar results were also obtained for the 1100 °C 24 h and 1300 °C 12 h samples. This uncertainty in the Cu_z-position entails a notable uncertainty in the calculated Cu-O4 distance.

The Cu occupancy increases slightly from 0.306 when annealing at 1100 °C to 0.322 when annealing at 1400 °C. This occupancy is close the previously reported value of 0.314 for single crystalline $Sr_5(PO_4)_3(CuO_2)_{1/3}$. At the same time, the O4 occupancy has a peak of 0.993 when annealing at 1300 °C, and is around 0.95 for the 1100 and 1400 °C samples. It can be noted that the O4 occupancy of the synthesized samples is clearly higher than in single crystalline $Sr_5(PO_4)_3(CuO_2)_{1/3}$, where it is 0.7 [27].

Given that the Wyckoff position for both the Cu- and O4-site has a multiplicity of 2, the ratio between Cu and O4 in the previously reported structure of $Sr_5(PO_4)_3(CuO_2)_{1/3}$ is 1:2, while the Cu:O4 ratio for the samples made using synthesis method 1 is rather 1:3. This suggests that the samples made using synthesis method 1 have a structure different of that for single crystalline $Sr_5(PO_4)_3(CuO_2)_{1/3}$. The larger ratio between oxygen vs copper also indicates that Cu^{2+} might be present in the synthesised structure.

It can also be noted that the ratio between strontium, phosphorus and copper in the calculated structures is approximately 5:3:0.32, while it was 5.05:3:1 between the initial reactants. It thus appears as if not all of the copper goes into the strontium apatite during the synthesis. There were indications after inspection that some of the copper might have diffused into the alumina crucible the pellets were placed in, or evaporated onto the surrounding walls of the tube furnace.

Regarding the isotropic displacement parameter, B, the calculated values differ for the different annealing temperatures, and some values stands out as being unreasonable large, especially on the O4-site for the 1300 °C and 1400 °C samples. These large values might indicate disorder in the structure [40].

Figure 5.5 shows the Rietveld refinement of the 1400 °C 6h sample from synthesis method 1.

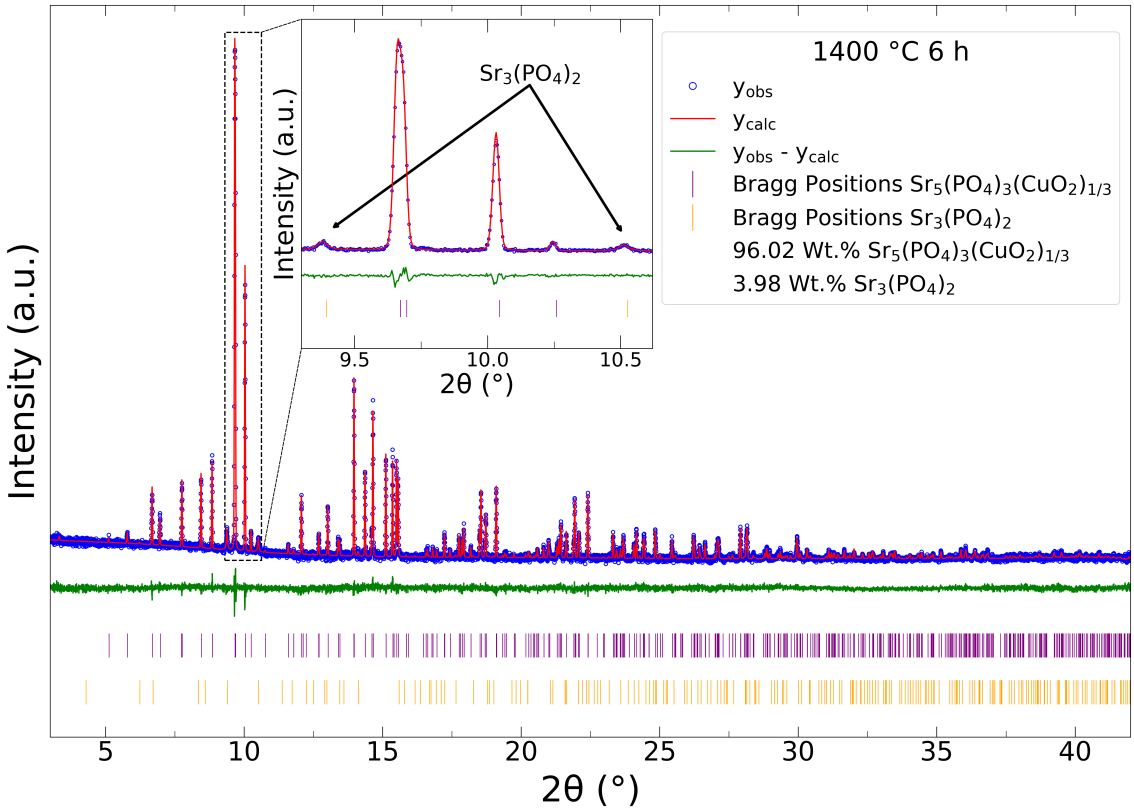

Figure 5.5: Rietveld refinement from synchrotron PXRD data on a sample made with synthesis method 1, annealed at 1400 °C for 6 h. The inset shows the two main peaks originating from the strontium phosphate impurity phase, as well as the main peaks of the copper-doped strontium apatite phase. This was also the most successful sample in terms of achieving the highest weight percentage of the copper-doped strontium apatite phase at 96.02 %.

Table 5.2 shows the structural information of the copper-doped strontium apatite phase from the 1400 °C 6h sample, and the corresponding structure is visualised in Figure 5.6.

Table 5.2: Atomic positions, occupancies, isotropic displacement parameters and Wyckoff positions for the different atomic sites from the Rietveld refinement of the 1400 °C 6 h sample made with synthesis method 1. Cells marked with dark grey correspond to non-refined values. The value within parentheses denotes the uncertainty, and is the estimated standard deviation calculated in TOPAS, multiplied by a factor of three.

Atomic Parameters							
Site	Species	Wyckoff Position	x	y	z	Occupancy	B_{iso} (Å^2)
Sr1	Sr^{2+}	4f	1/3	2/3	−0.00173(53)	1.0	0.93(4)
Sr2	Sr^{2+}	6h	0.25928(23)	0.01340(31)	1/4	1.0	1.06(4)
Cu	Cu^{+}	2a	0	0	0	0.322(8)	0.87(30)
P	P^{5+}	6h	0.36715(60)	0.39895(60)	1/4	1.0	0.85(12)
O1	O^{2-}	6h	0.48081(136)	0.33323(135)	1/4	1.0	1.44(44)
O2	O^{2-}	6h	0.45806(156)	0.58603(147)	1/4	1.0	1.44(44)
O3	O^{2-}	12i	0.26179(87)	0.34816(87)	0.07272(98)	1.0	1.44(44)
O4	O^{2-}	2a	0	0	1/4	0.948(35)	4.50(77)

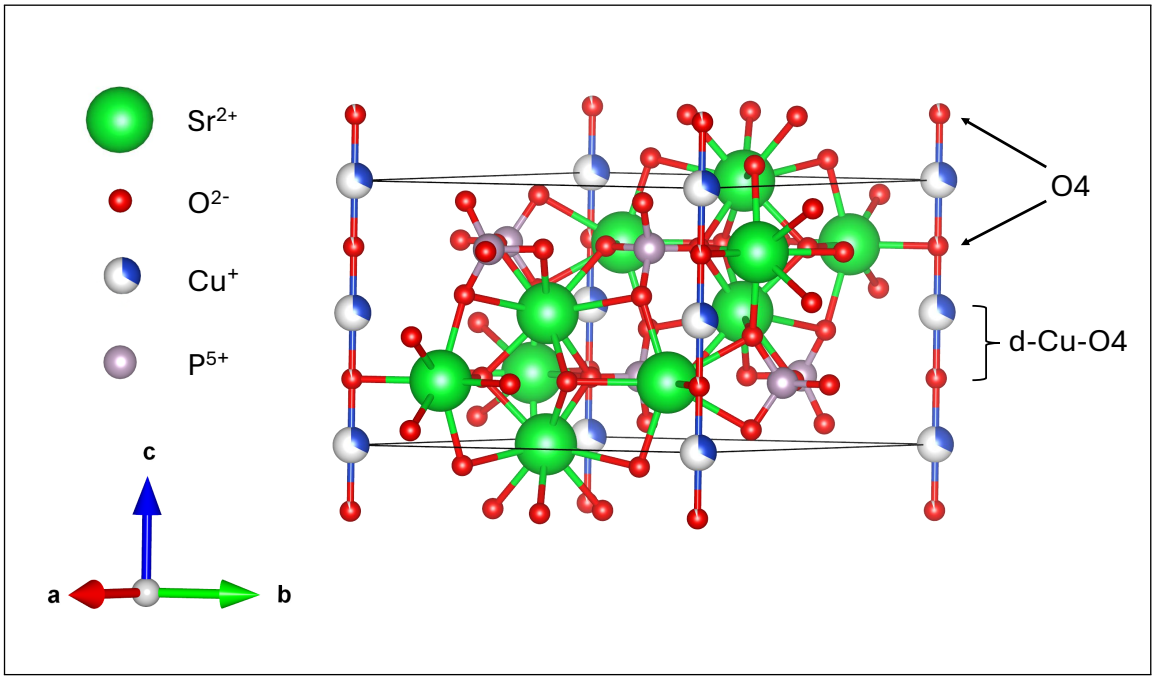

Figure 5.6: The structure of the 1400 °C sample from the Rietveld refinement, where the distance between the copper ion and O4-oxygen is highlighted. Visualised in VESTA.

The Rietveld refinement of the 1400 °C 6 h annealing sample made using synthesis method 2, which was used for the IR-measurements, also had $Sr_5(PO_4)_3(CuO_2)_{1/3}$ present as the main phase with a weight percentage of 93.73 % and $Sr_3(PO_4)_2$ as

a minor impurity phase. More details of this refinement can be found in Appendix B.

5.5 Infrared Spectroscopy

The result of the IR-measurements on the samples from synthesis method 2 is given below. The samples made with synthesis method 2 are assumed to be representative also for the samples made with synthesis method 1, due to the similarity in the methods, the similar colour of the obtained samples, as well as the similar results from the Rietveld refinements for each synthesis method.

Previous infrared (IR) absorption measurements performed on strontium hydroxyapatite, $Sr_{10}(PO_4)_6(OH)_2$, show bands at 539– and 3593 cm^{-1}, respectively attributed to an OH–libration and OH-stretch mode [55]. This can be compared to the IR absorbance spectra of the samples made using synthesis method 2, shown in Figure 5.8 (fingerprint region) and Figure 5.7 (OH-stretch region). None of the samples shows the characteristic bands at 539– or 3593 cm^{-1}, marked with red lines in the Figure 5.8 and 5.7, indicating an absence of OH-bonds giving rise to libration– and stretching motions in the synthesised structures.

Moreover, the samples show bands at 1070, 943, 590, 561 and 459 cm^{-1}, all being typical to modes originating from the $PO_4{}^{3-}$-group when measuring on strontium hydroxyapatite, $Sr_{10}(PO_4)_6(OH)_2$ [55].

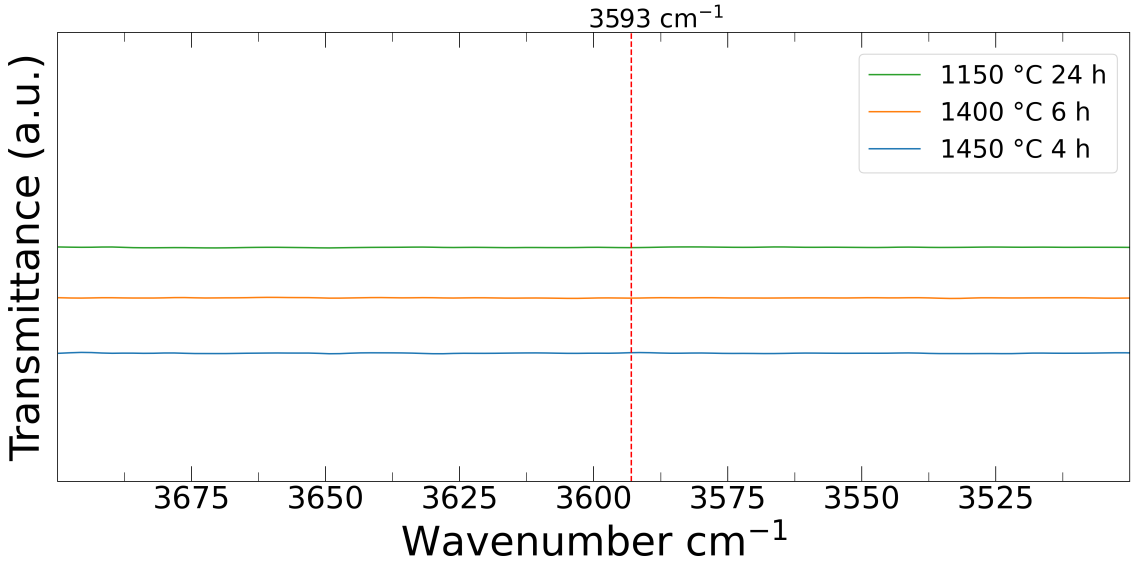

Figure 5.7: IR spectra in the OH-stretch region for samples synthesized with method 2 and annealed at 1150 °C 24 h, 1400 °C 6 h and 1450 °C 4 h respectively. Note that none of the samples shows a band at 3593 cm^{-1}, which corresponds to the OH-stretch present in strontium hydroxyapatite, $Sr_{10}(PO_4)_6(OH)_2$ [55].

The band marked at 784 cm^{-1} in Figure 5.8 matches well with 785 cm^{-1}, which has previously been attributed to a Cu-O stretch in oxocuprate ions (the $[OCuO]^{3-}$-units in the one-dimensional channels), when measuring on single crystals of $Sr_5(PO_4)_3(CuO_2)_{1/3}$ [27]. This suggests that some form of oxocuprate ion is present in the samples made with synthesis method 2.

It can also be noted that this band is shifted to a smaller wave number for the sample synthesised at 1150 °C. If a shorter Cu-O4 distance is assumed to correspond to a stronger bond, and if a stronger bond corresponds to a higher vibrational frequency (and vice versa) [27], then the lower wave number for the 1150 °C sample could indicate a larger Cu-O4 distance. This is however contradicting the calculated Cu-O4 distance from the Rietveld refinement, with the 1150 °C sample having the shortest Cu-O4 distance at 1.822 Å. Although, as discussed in Section 5.4, there is a substantial uncertainty in the calculated Cu-O4 distance. The uncertainty in the oxidation state of the copper-ions and the Cu-O4 distance, makes it difficult to discern what type of oxocuprate units that are present in the synthesised structures.

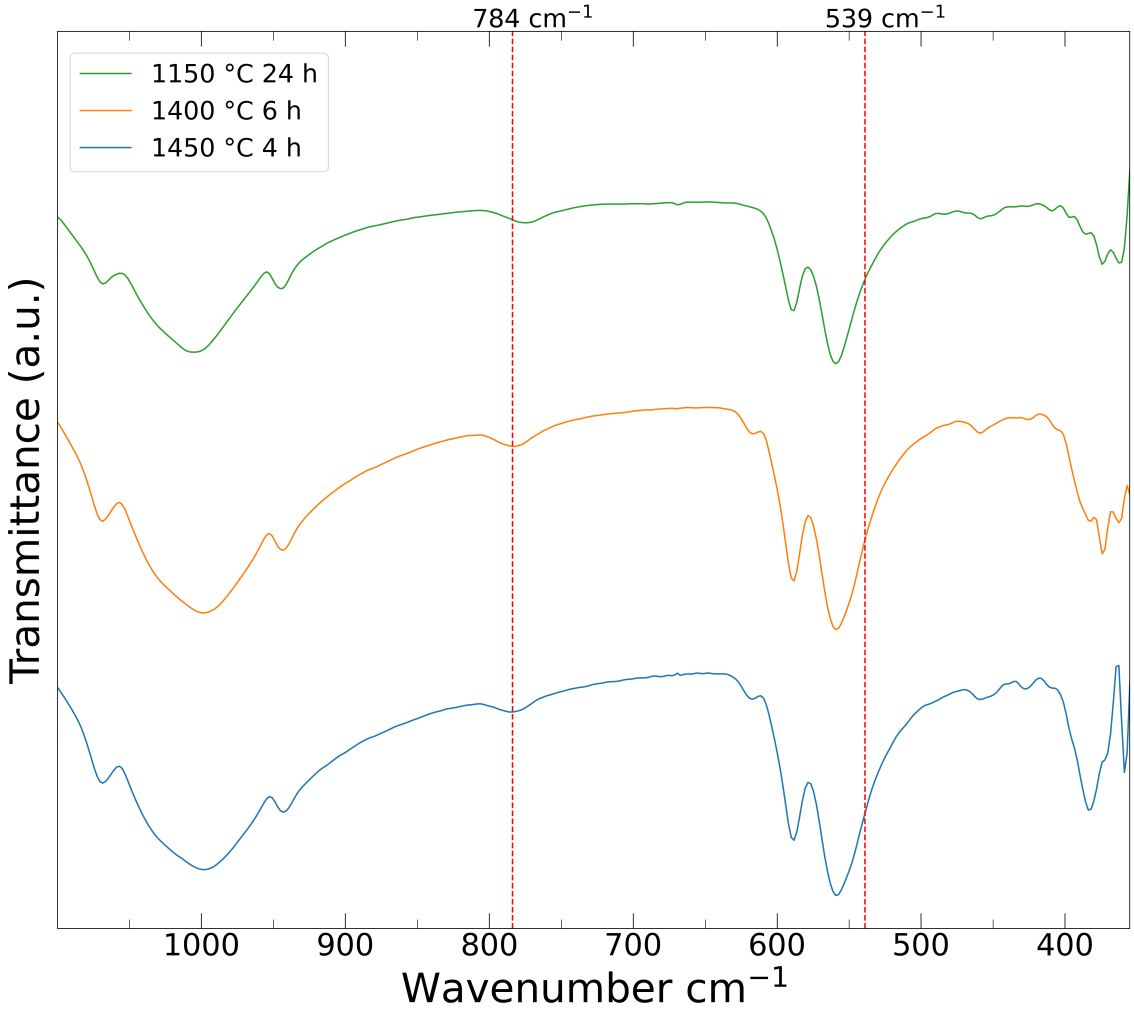

Figure 5.8: IR spectra in the fingerprint region for samples synthesized by method 2 and annealed at 1150 °C 24 h, 1400 °C 6 h and 1450 °C 4 h respectively. None of the sample show bands at 539 cm^{-1}, which corresponds to the OH-libration mode in strontium hydroxyapatite, $Sr_{10}(PO_4)_6(OH)_2$. There is also a band present at 784 cm^{-1}, which corresponds well to the band present at 785 cm^{-1} in $Sr_5(PO_4)_3(CuO_2)_{1/3}$, which has been proposed to originate from the $[OCuO]^{-3}$- units in the one-dimensional channels [27].

Chapter 6

Conclusions and Outlook

The results show it is possible to synthesise a purple-coloured copper doped strontium apatite structure, using high temperature ceramic methods. The Rietveld refinements suggest the most favourable synthesis condition is by annealing at 1400 °C for 6 hours followed by air quenching, creating a copper doped strontium apatite structure as the majority phase (96.02 Wt.%) and $Sr_3(PO_4)_2$ as a minor side-phase (3.98 Wt.%). The calculated bond length between the Cu and O in the one-dimensional channels along the c-axis was found to be 1.825 Å when annealing at 1400 °C. This is in well agreement with previous reports of 1.825 Å [27], as well as with linearly coordinated Cu(I)-O bonds in $AlCuO_2$ (1.86 Å) [53] and $FeCuO_2$ (1.84 Å) [54]. However, the exact structure of the material synthesised with the methods used in this project remains to be determined, as indicated by the occupancy on the O4-position, as well as the potential disorder indicated by the Debye-Waller factors. Moreover, the synthesised copper-doped strontium apatite was discovered to melt at 1500 °C.

Infrared spectroscopy measurements indicate no bands at 539 cm^{-1} and 3593 cm^{-1} for the synthesised structure. These are bands which have been attributed to OH-bonds in strontium hydroxyapatite, $Sr_{10}(PO_4)_6(OH)_2$, located in the hexagonal one-dimensional channels of $P6_3/m$-apatites [26]. The synthesis methods used thus seems to result in a copper-doped strontium apatite structure where hydroxyl groups are not present. The bands present at 784 cm^{-1} indicates that some type of oxocuprate ion, giving rise to a Cu-O stretch, is present in the synthesised structures. Although, it is difficult to determine exactly what type of oxocuprate ion of from the obtained data.

In order to gain further insights into the structure of the synthesised copper-doped strontium apatite, additional characterisation techniques, such as neutron diffraction could be used, to further elucidate the presence of hydrogen. Electron paramagnetic spectroscopy, as well as X-ray photoelectron spectroscopy, may also be utilised to investigate the oxidation state of the copper ions in the apatite structure.

Finally, efforts to optimise the synthesis method towards obtaining phase pure copper-doped strontium apatite is encouraged. Since the amount of copper was substantially lower in the final product compared to the reactants, it could be of interest to evaluate reactions where the copper ratio among the reactants is increased. Further optimising annealing temperature and dwelling time might also help in order to reach a more phase pure sample. If achieved, the phase pure copper-doped strontium apatite could then be used as a foundation, for investigating how to alter the oxygen content and oxidation state of the copper in the structure.

References

1. Moore E and Smart LE. Solid state chemistry: an introduction. eng. Fifth edition. Boca Raton London New York: CRC Taylor & Francis Group, 2021
2. Rom CL, Smaha RW, O'Donnell S, Dugu S, and Bauers SR. Emerging magnetic materials for electric vehicle drive motors. en. MRS Bulletin 2024 Jul; 49:738–50. DOI: 10.1557/s43577-024-00743-4. Available from: https://link.springer.com/10.1557/s43577-024-00743-4 [Accessed on: 2026 Mar 3]
3. Boiko O and Stryczewska HD. Superconductivity and Cryogenics in Medical Diagnostics and Treatment: An Overview of Selected Applications. en. Applied Sciences 2025 Nov; 15:12579. DOI: 10.3390/app152312579. Available from: https://www.mdpi.com/2076-3417/15/23/12579 [Accessed on: 2026 Mar 3]
4. Lee S, Kim JH, and Kwon YW. The First Room-Temperature Ambient-Pressure Superconductor. arXiv:2307.12008 [cond-mat]. 2023 Jul. DOI: 10.48550/arXiv.2307.12008. Available from: http://arxiv.org/abs/2307.12008 [Accessed on: 2026 Jan 20]
5. Padavic-Callaghan K. The viral superconductor. New Scientist 2023 Dec; 260:18. DOI: 10.1016/S0262-4079(23)02323-0. Available from: https://www.sciencedirect.com/science/article/pii/S0262407923023230 [Accessed on: 2025 Jun 16]
6. Kim SW, Wang K, Chen S, Conway LJ, Pascut GL, Errea I, Pickard CJ, and Monserrat B. On the dynamical stability of copper-doped lead apatite. en. npj Computational Materials 2024 Jan; 10:16. DOI: 10.1038/s41524-024-01206-9. Available from: https://www.nature.com/articles/s41524-024-01206-9 [Accessed on: 2025 Jun 16]
7. Zhu S, Wu W, Li Z, and Luo J. First-order transition in LK-99 containing Cu2S. en. Matter 2023 Dec; 6:4401–7. DOI: 10.1016/j.matt.2023.11.001. Available from: https://linkinghub.elsevier.com/retrieve/pii/S2590238523005647 [Accessed on: 2026 Jan 21]
8. Lee S, Kim J, Kim HT, Im S, An S, and Auh KH. Superconductor Pb_{10-x}Cu_x(PO_4)_6O showing levitation at room temperature and atmospheric pressure and mechanism. arXiv:2307.12037 [cond-mat]. 2023 Aug. DOI: 10.48550/arXiv.2307.12037. Available from: http://arxiv.org/abs/2307.12037 [Accessed on: 2026 Mar 25]
9. Cho B, Park J, Yun D, Seo J, and Park K. Exploration of superconductivity in LK-99 synthesized under different cooling conditions. Current Applied Physics 2024 Jun; 62:22–8. DOI: 10.1016/j.cap.2024.03.007. Available from: https:

//www.sciencedirect.com/science/article/pii/S1567173924000531 [Accessed on: 2025 Jun 16]
10. Scheifers JP, Richardson AJD, Lin H, Niu H, Daniels LM, Gaultois MW, Alaria J, Robertson CM, Claridge JB, and Rosseinsky MJ. Superstructure Formation through Coupled Anion and Cation Ordering in Cu-Substituted Lead Oxyapatites. Chemistry of Materials 2025 May; 37:3088–99. DOI: 10.1021/acs.chemmater.4c03130. Available from: https://doi.org/10.1021/acs.chemmater.4c03130 [Accessed on: 2025 Nov 24]
11. Panas I. Postmortem analysis and possible rebirth of LK-99. 2024 Sep. DOI: 10.48550/arXiv.2410.03722. Available from: http://arxiv.org/abs/2410.03722 [Accessed on: 2025 Jun 16]
12. Morrison G, Adams EN, Jones VG, Zamorano KP, and Zur Loye HC. Investigating Copper Doping in Lead Oxyapatite: Flux Growth of Copper-Containing Pb_{10} $(PO_4)_6$ O Single Crystals. en. Chemistry of Materials 2025 Jul; 37:4894–900. DOI: 10.1021/acs.chemmater.5c01065. Available from: https://pubs.acs.org/doi/10.1021/acs.chemmater.5c01065 [Accessed on: 2026 Jan 20]
13. Tallon JL. Oxygen in High-Tc Cuprate Superconductors. en. *Frontiers in Superconducting Materials*. Ed. by Narlikar AV. Berlin, Heidelberg: Springer, 2005 :295–330. DOI: 10.1007/3-540-27294-1_7. Available from: https://doi.org/10.1007/3-540-27294-1_7 [Accessed on: 2025 Jun 16]
14. Radii for Sr. Available from: http://abulafia.mt.ic.ac.uk/shannon/radius.php?Element=Sr [Accessed on: 2026 Jan 20]
15. Radii for Pb. Available from: http://abulafia.mt.ic.ac.uk/shannon/radius.php?Element=Pb [Accessed on: 2026 Jan 20]
16. Roycroft PD and Cuypers M. The Etymology of The Mineral Name 'Apatite': A Clarification. Irish Journal of Earth Sciences 2015; 33:71–5. DOI: 10.3318/ijes.2015.33.71. Available from: https://www.jstor.org/stable/10.3318/ijes.2015.33.71 [Accessed on: 2025 Nov 20]
17. Zhang C, Chen C, Li Z, and Shen AH. Chemical Composition and Spectroscopic Characteristics of Alexandrite Effect Apatite from the Akzhailyau Mountains of Kazakhstan. en. Minerals 2023 Aug; 13:1139. DOI: 10.3390/min13091139. Available from: https://www.mdpi.com/2075-163X/13/9/1139 [Accessed on: 2026 Mar 3]
18. Siddiqui HA, Pickering KL, and Mucalo MR. A Review on the Use of Hydroxyapatite-Carbonaceous Structure Composites in Bone Replacement Materials for Strengthening Purposes. en. Materials 2018 Oct; 11:1813. DOI: 10.3390/ma11101813. Available from: https://www.mdpi.com/1996-1944/11/10/1813 [Accessed on: 2025 Nov 19]
19. Duminis T, Shahid S, and Hill RG. Apatite Glass-Ceramics: A Review. English. Frontiers in Materials 2017 Jan; 3. DOI: 10.3389/fmats.2016.00059. Available from: https://www.frontiersin.org/journals/materials/articles/10.3389/fmats.2016.00059/full [Accessed on: 2025 Nov 19]
20. Kamiya H, Kato K, Xin Y, Xu Y, and Shirai T. Pt/facet-Engineered Hydroxyapatite Co-Catalyst for Highly Efficient Hydrolysis of Ammonia Borane. en. Catalysis Letters 2024 Nov; 154:6012–21. DOI: 10.1007/s10562-024-04773-

0. Available from: https://link.springer.com/10.1007/s10562-024-04773-0 [Accessed on: 2025 Nov 19]
21. Hughes JM. The many facets of apatite. en. American Mineralogist 2015 May; 100:1033–9. DOI: 10.2138/am-2015-5193. Available from: https://www.degruyter.com/document/doi/10.2138/am-2015-5193/html [Accessed on: 2026 Mar 3]
22. White TJ and ZhiLi D. Structural derivation and crystal chemistry of apatites. en. Acta Crystallographica Section B Structural Science 2003 Feb; 59:1–16. DOI: 10.1107/S0108768102019894. Available from: https://journals.iucr.org/paper?S0108768102019894 [Accessed on: 2025 Nov 20]
23. Balhuc S, Campian R, Labunet A, Negucioiu M, Buduru S, and Kui A. Dental Applications of Systems Based on Hydroxyapatite Nanoparticles—An Evidence-Based Update. en. Crystals 2021 Jun; 11:674. DOI: 10.3390/cryst11060674. Available from: https://www.mdpi.com/2073-4352/11/6/674 [Accessed on: 2025 Jun 16]
24. Saito K, Kagawa S, Ogasawara M, and Kato S. Multiple incorporation of copper and iron ions into the channel of hydroxyapatite. Journal of Solid State Chemistry 2023 Jan; 317:123673. DOI: 10.1016/j.jssc.2022.123673. Available from: https://www.sciencedirect.com/science/article/pii/S0022459622007988 [Accessed on: 2025 Jun 16]
25. Sudarsanan K and Young RA. Structure of strontium hydroxide phosphate, Sr_5 $(PO_4$ $)_3$ OH. en. Acta Crystallographica Section B Structural Crystallography and Crystal Chemistry 1972 Dec; 28:3668–70. DOI: 10.1107/S0567740872008544. Available from: https://journals.iucr.org/paper?S0567740872008544 [Accessed on: 2026 Feb 5]
26. Andrade AVC de, Silva JCZ da, Paiva-Santos CO, Weber C, Santos Utuni VH dos, Tebcherani SM, Borges CPF, Costa E da, Manent SM, and Cavalcanti AGC. Synthesis and Crystal Phase Evaluation of Hydroxylapatite Using the Rietveld-Maximum Entropy Method. en. *28th International Conference on Advanced Ceramics and Composites B: Ceramic Engineering and Science Proceedings*. John Wiley & Sons, Ltd, 2004 :639–45. DOI: 10.1002/9780470291191.ch97. Available from: https://onlinelibrary.wiley.com/doi/abs/10.1002/9780470291191.ch97 [Accessed on: 2025 Nov 20]
27. Kazin PE, Karpov AS, Jansen M, Nuss J, and Tretyakov YD. Crystal Structure and Properties of Strontium Phosphate Apatite with Oxocuprate Ions in Hexagonal Channels. en. Zeitschrift für anorganische und allgemeine Chemie 2003 Feb; 629:344–52. DOI: 10.1002/zaac.200390055. Available from: https://onlinelibrary.wiley.com/doi/10.1002/zaac.200390055 [Accessed on: 2025 Apr 21]
28. Pogosova M and González L. Influence of anion substitution on the crystal structure and color properties of copper-doped strontium hydroxyapatite. en. Ceramics International 2018 Nov; 44:20140–7. DOI: 10.1016/j.ceramint.2018.07.307. Available from: https://linkinghub.elsevier.com/retrieve/pii/S0272884218320558 [Accessed on: 2026 Jan 23]
29. (International Tables) Volume A1 home page. en. text. Available from: https://it.iucr.org//A1a/ [Accessed on: 2026 Feb 12]

30. Gnesin GG. Revisiting the history of materials science on the origin and development of ceramic technology. en. Powder Metallurgy and Metal Ceramics 2012 Nov; 51:496–501. DOI: 10.1007/s11106-012-9460-z. Available from: http://link.springer.com/10.1007/s11106-012-9460-z [Accessed on: 2025 May 3]
31. Walker RP. Synchrotron radiation. 1994. DOI: 10.5170/CERN-1994-001.437. Available from: https://cds.cern.ch/record/398429 [Accessed on: 2025 Nov 9]
32. Sedigh Rahimabadi P, Khodaei M, and Koswattage KR. Review on applications of synchrotron-based X-ray techniques in materials characterization. en. X-Ray Spectrometry 2020 May; 49:348–73. DOI: 10.1002/xrs.3141. Available from: https://analyticalsciencejournals.onlinelibrary.wiley.com/doi/10.1002/xrs.3141 [Accessed on: 2025 Nov 9]
33. Synchrotron Radiation. en-GB. Available from: https://www.kth.se/relax/infrastructures/synchrotron-radiation-1.1386163 [Accessed on: 2025 Nov 9]
34. Soleil Synchrotron E3S. Deutsch: Schema des französischen Synchrotron Soleil. Der abgebildete große Ring ist das Synchrotron, ein Teilchenbeschleuniger, der Elektronen auf Geschwindigkeiten nahe der Lichtgeschwindigkeit bringt. Das innere Oval ist eine Strecke zur Vorbeschleunigung, in der das Elektron bereits über 99% der Lichtgeschwindigkeit erreicht. In den acht „Armen“ befinden sich wissenschaftliche Geräte, die die Bremsstrahlung der in den Kurven abgelenkten Elektronen auffangen und analysieren. 2005 Oct. Available from: https://commons.wikimedia.org/wiki/File:Sch%C3%A9ma_de_principe_du_synchrotron.jpg [Accessed on: 2025 Nov 11]
35. About us | French national synchrotron facility. Available from: https://www.synchrotron-soleil.fr/en/about-us [Accessed on: 2025 Nov 11]
36. Gavaghan H. What is a synchrotron? en. Nature 2001 Apr; 410:722–2. DOI: 10.1038/35070715. Available from: https://www.nature.com/articles/35070715 [Accessed on: 2025 Nov 11]
37. Kaduk JA, Billinge SJL, Dinnebier RE, Henderson N, Madsen I, Černý R, Leoni M, Lutterotti L, Thakral S, and Chateigner D. Powder diffraction. en. Nature Reviews Methods Primers 2021 Nov; 1:77. DOI: 10.1038/s43586-021-00074-7. Available from: https://www.nature.com/articles/s43586-021-00074-7 [Accessed on: 2025 Nov 27]
38. Cullity BD and Stock SR. Elements of X-ray diffraction. eng. 3. ed., new internat. ed. Harlow: Pearson Education, 2014
39. Evans JSO and Evans IR. Structure Analysis from Powder Diffraction Data: Rietveld Refinement in Excel. en. Journal of Chemical Education 2021 Feb; 98:495–505. DOI: 10.1021/acs.jchemed.0c01016. Available from: https://pubs.acs.org/doi/10.1021/acs.jchemed.0c01016 [Accessed on: 2025 Nov 26]
40. Runčevski T. Rietveld Refinement Practical Powder Diffraction Pattern Analysis using TOPAS. By Robert E. Dinnebier, Andreas Leineweber and John S. O. Evans. De Gruyter, 2019. Pp. 331. Price (paperback) EUR 69.95, USD 80.99, GBP 63.50. ISBN 978-3-11-045621-9, e-ISBN (PDF) 978-3-11-046138-

1. en. Journal of Applied Crystallography 2019 Oct; 52:1238–9. DOI: 10.1107/S1600576719011178. Available from: https://journals.iucr.org/j/issues/2019/05/00/xo5026/ [Accessed on: 2025 Nov 26]
41. Wachs IE and Bañares MA, eds. Springer Handbook of Advanced Catalyst Characterization. en. Springer Handbooks. Cham: Springer International Publishing, 2023. DOI: 10.1007/978-3-031-07125-6. Available from: https://link.springer.com/10.1007/978-3-031-07125-6 [Accessed on: 2025 May 4]
42. Rietveld HM. A profile refinement method for nuclear and magnetic structures. en. Journal of Applied Crystallography 1969 Jun; 2:65–71. DOI: 10.1107/S0021889869006558. Available from: https://journals.iucr.org/paper?S0021889869006558 [Accessed on: 2026 Feb 16]
43. McCusker LB, Von Dreele RB, Cox DE, Louër D, and Scardi P. Rietveld refinement guidelines. en. Journal of Applied Crystallography 1999 Feb; 32:36–50. DOI: 10.1107/S0021889898009856. Available from: https://journals.iucr.org/paper?S0021889898009856 [Accessed on: 2025 Nov 26]
44. Hill RJ and Howard CJ. Quantitative phase analysis from neutron powder diffraction data using the Rietveld method. en. Journal of Applied Crystallography 1987 Dec; 20:467–74. DOI: 10.1107/S0021889887086199. Available from: https://journals.iucr.org/paper?S0021889887086199 [Accessed on: 2026 Jan 30]
45. Scarlett NVY and Madsen IC. Quantification of phases with partial or no known crystal structures. en. Powder Diffraction 2006 Dec; 21:278–84. DOI: 10.1154/1.2362855. [Accessed on: 2026 Jan 30]
46. Al-Amin K, Kawsar M, Bhuiyan Mamun MTR, and Hossain MS. Fourier transform infrared spectroscopic technique for analysis of inorganic materials: a review. en. Nanoscale Advances 2025; 7:6677–702. DOI: 10.1039/D5NA00522A. Available from: https://pubs.rsc.org/en/content/articlelanding/2025/na/d5na00522a [Accessed on: 2025 Nov 23]
47. Blum MM and John H. Historical perspective and modern applications of Attenuated Total Reflectance – Fourier Transform Infrared Spectroscopy (ATR-FTIR). en. Drug Testing and Analysis 2012; 4:298–302. DOI: 10.1002/dta.374. [Accessed on: 2025 Nov 24]
48. DIFFRAC.TOPAS. en. Available from: https://www.bruker.com/en/products-and-solutions/diffractometers-and-x-ray-microscopes/x-ray-diffractometers/diffrac-suite-software/diffrac-topas.html [Accessed on: 2025 Jun 16]
49. ICSD - Details on Search Result. Available from: https://icsd-fiz-karlsruhe-de.proxy.lib.chalmers.se/display/details.xhtml [Accessed on: 2026 Feb 12]
50. Sugiyama K and Tokonami M. The crystal structure refinements of the strontium and barium orthophosphates. Mineralogical Journal 1990; 15:141–6. DOI: 10.2465/minerj.15.141
51. Stephens PW. Phenomenological model of anisotropic peak broadening in powder diffraction. en. Journal of Applied Crystallography 1999 Apr; 32:281–9.

DOI: 10.1107/S0021889898006001. Available from: https://journals.iucr.org/paper?S0021889898006001 [Accessed on: 2026 Mar 3]

52. Pogosova M, Provotorov D, Eliseev A, Jansen M, and Kazin P. Synthesis and characterization of the Bi-for-Ca substituted copper-based apatite pigments. en. Dyes and Pigments 2015 Feb; 113:96–101. DOI: 10.1016/j.dyepig.2014.07.038. Available from: https://linkinghub.elsevier.com/retrieve/pii/S0143720814003210 [Accessed on: 2026 Jan 23]
53. Materials Data on AlCuO2 by Materials Project. English. Tech. rep. mp-3098. LBNL Materials Project; Lawrence Berkeley National Laboratory (LBNL), Berkeley, CA (United States), 2020 Jul. DOI: 10.17188/1205315. Available from: https://www.osti.gov/biblio/1205315 [Accessed on: 2026 Jan 12]
54. Materials Data on FeCuO2 by Materials Project. English. Tech. rep. mp-510281. LBNL Materials Project; Lawrence Berkeley National Laboratory (LBNL), Berkeley, CA (United States), 2020 Jul. DOI: 10.17188/1262873. Available from: https://www.osti.gov/biblio/1262873 [Accessed on: 2026 Jan 12]
55. González-Díaz P and Santos M. Infrared spectra of strontium, lead and barium apatites. en. Spectrochimica Acta Part A: Molecular Spectroscopy 1978 Jan; 34:241–6. DOI: 10.1016/0584-8539(78)80140-8. Available from: https://linkinghub.elsevier.com/retrieve/pii/0584853978801408 [Accessed on: 2025 Jun 5]

Appendix A

Additional Rietveld refinements on samples made with synthesis method 1.

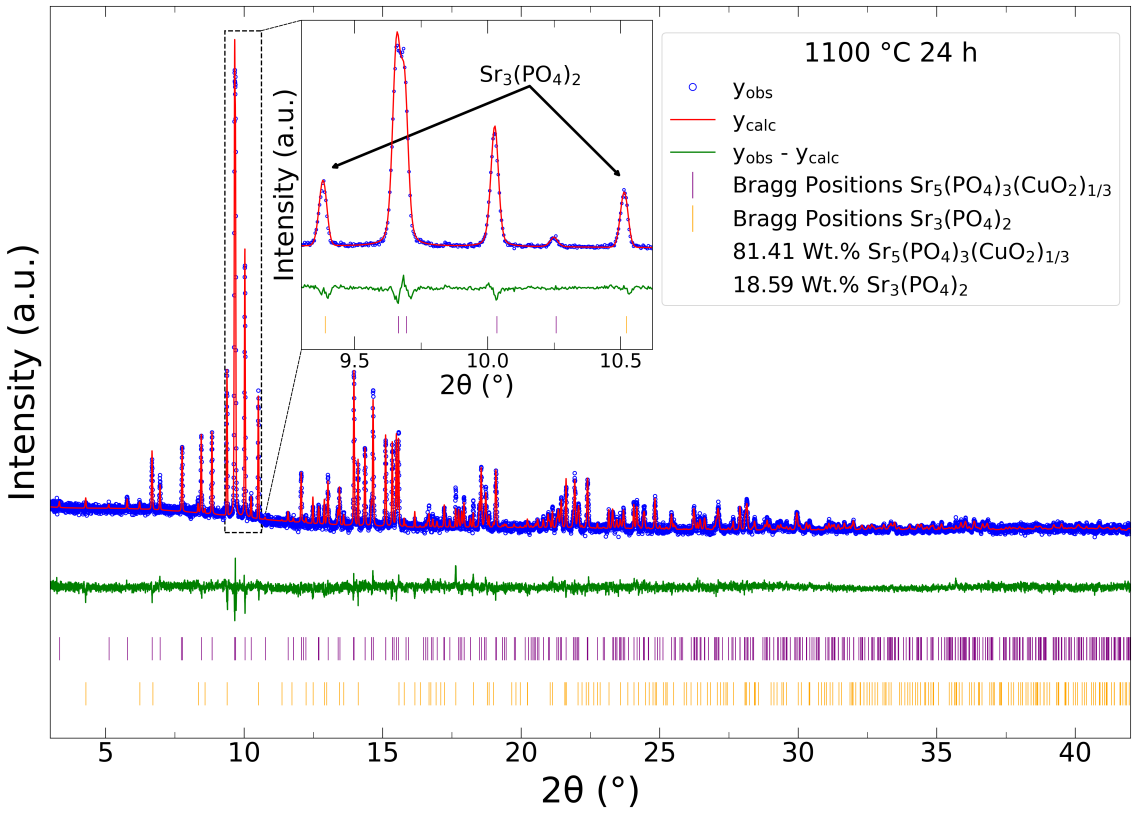

Figure A.1: Rietveld refinement from synchrotron PXRD data on the sample made with synthesis method 1 and annealed at 1100 °C for 24 hours. The zoomed in area shows the two main peaks originating from the strontium phosphate impurity phase.

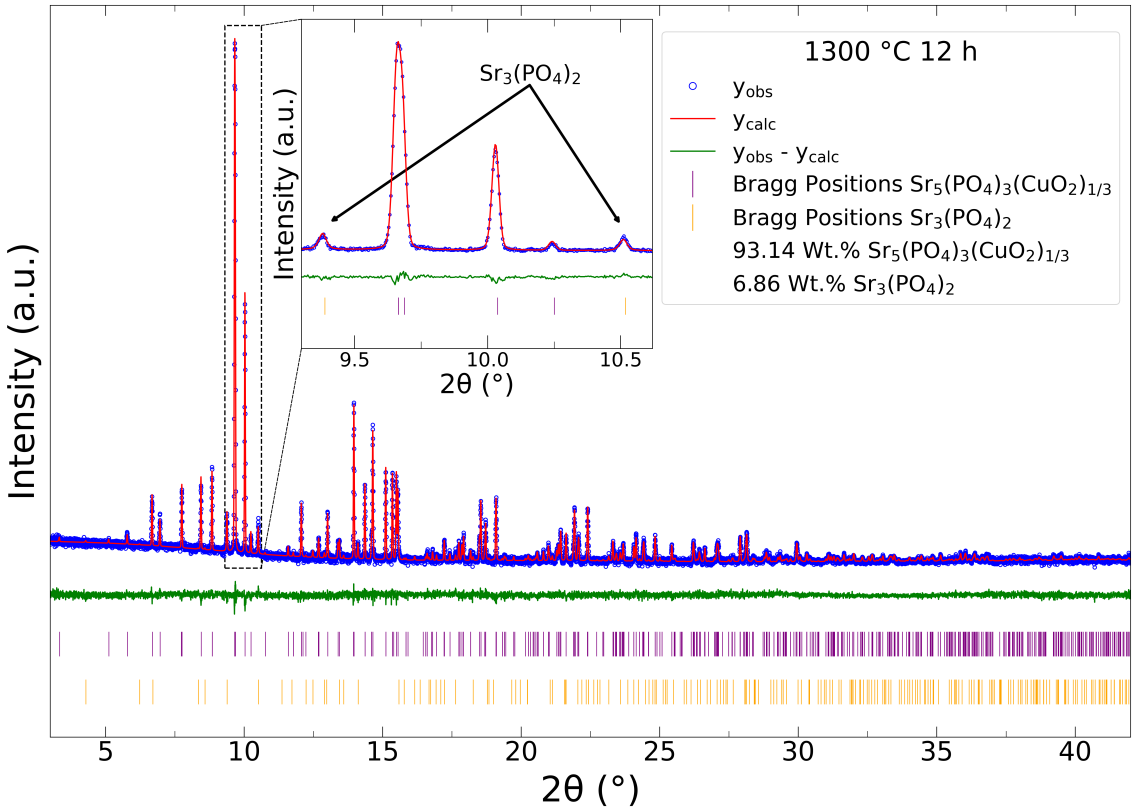

Figure A.2: Rietveld refinement from synchrotron PXRD data on the sample made with synthesis method 1 and annealed at 1300 °C for 12 hours. The zoomed in area shows the two main peaks originating from the strontium phosphate impurity phase.

Appendix B

Rietveld refinement done on the sample made with synthesis method 2 and annealed at 1400 °C.

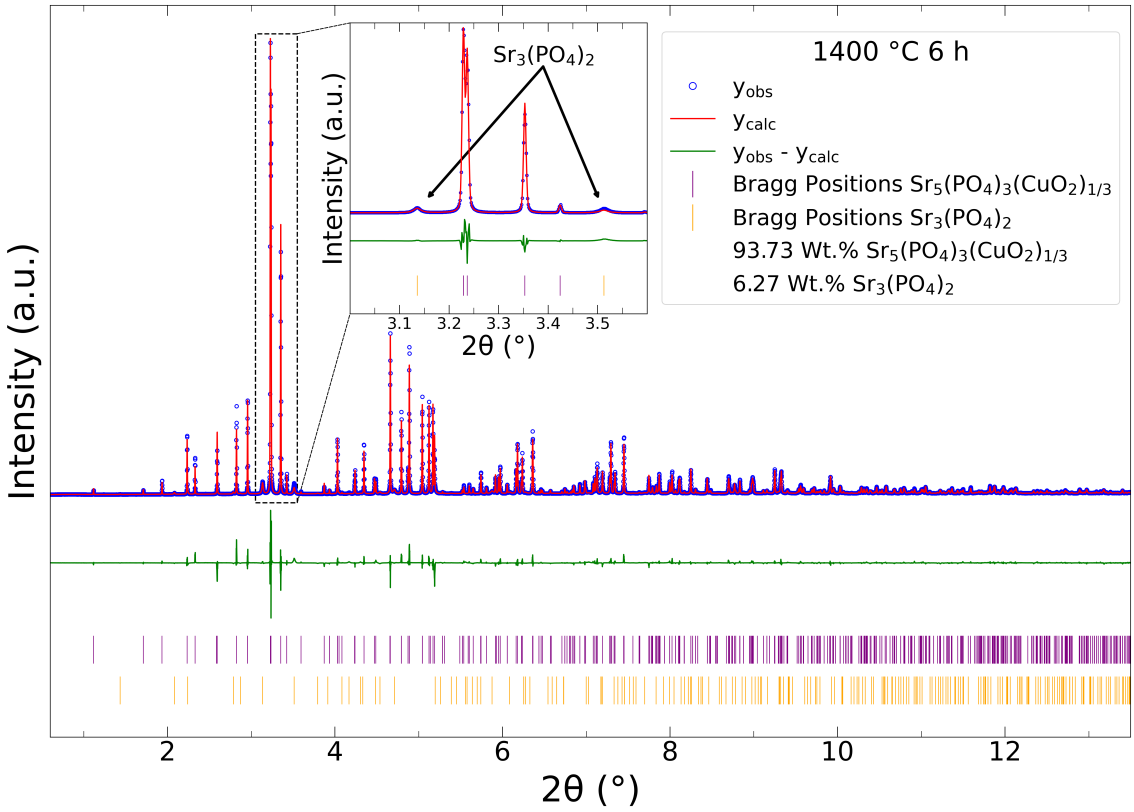

Figure B.1: Rietveld refinement from synchrotron PXRD data on the sample made with synthesis method 2 and annealed at 1400 °C for 6 hours. The zoomed in area shows the two main peaks originating from the strontium phosphate impurity phase.

Table B.1: Summary of the Rietveld refinement done on the sample from synthesis method 2 and annealed at 1400 °C 6 hours. The uncertainty in the calculated values (values in the parenthesis) is given as the calculated standard deviation from TOPAS, multiplied by a factor of three.

Summary of Rietveld Refinements from Synchrotron PXRD Data	
$Sr_5(PO_4)_3(CuO_2)_{1/3}$ Space Group	$P6_3/m$
$Sr_3(PO_4)_2$ Space Group	$R\bar{3}m$
Annealing Temp & Time	1400 °C 6h
R_{wp}	12.93
GoF	2.72
Wt. % CuSrApt	93.73(48)
Wt. % $Sr_3(PO_4)_2$	6.27(48)

DEPARTMENT OF Chemistry and Chemical Engineering Chalmers University
CHALMERS UNIVERSITY OF TECHNOLOGY
Gothenburg, Sweden
www.chalmers.se

CHALMERS
UNIVERSITY OF TECHNOLOGY